Thermomechanical Analysis of Beam Dump Devices for the Large Hadron Collider

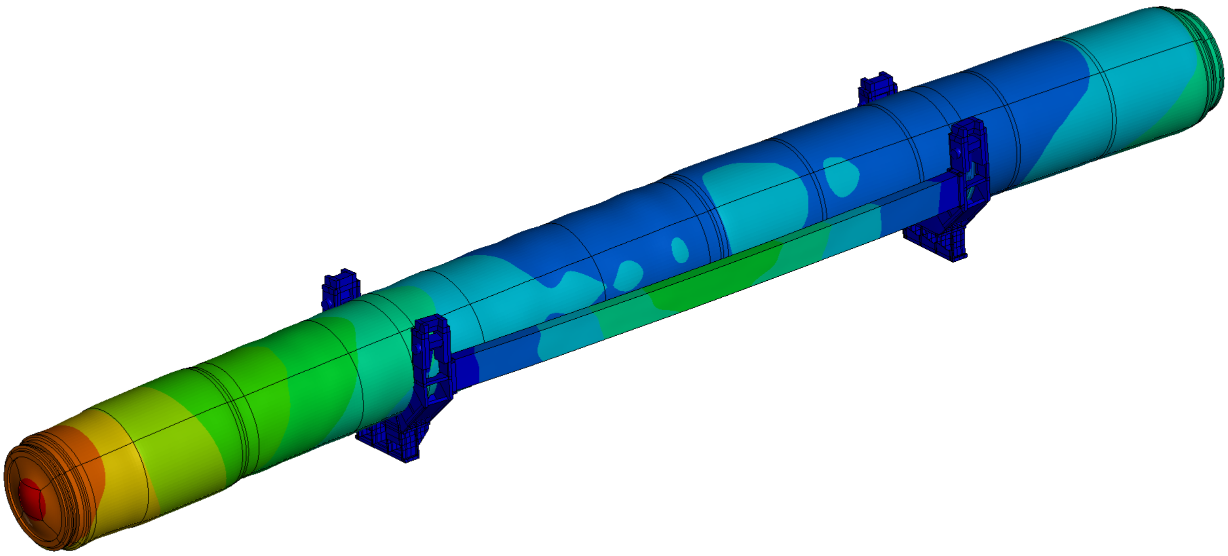

A Bachelor thesis by Jules Braken

HAN University of Applied Sciences – Faculty of Engineering and Automotive

In collaboration with the European Organisation for Nuclear Research (CERN)

03-06-2024

University:
HAN University of Applied Sciences
Faculty:
Automotive Engineering
Address:
Ruitenberglaan 29, 6826CC, Arnhem
Thesis Supervisor:
Jaap Janssens
Specialisation:
Structural Design

Hosting Organisation:
European Organisation for Nuclear Research (CERN)
Department:
SY-STI-TCD
Address:
Esplanade des Particules 1, 1211 Meyrin
Company Supervisor:
Asbjørn Lassen Lund

This bachelor thesis was made with LaTeX using Overleaf. The title page illustration was taken from a simulation in LS-DYNA®. Figures from simulations are outputs from LS-DYNA® and Ansys®, where graphs are post-processed in Excel and images constructed and edited with the help of Powerpoint.

Abstract

The Large Hadron Collider (LHC) is the most powerful accelerator at the European Organisation for Nuclear Research (CERN). It is used to perform fundamental physics research by colliding two counter-rotating proton beams after they have been accelerated to nearly the speed of light. The Target Dump Externals (TDE) are responsible for the safe absorption of the LHC particle beams in all possible scenarios, including instances of abnormal machine operation.

The LHC undergoes higher levels of stored energy in the particle beams with each operational run, leading to increased thermal loads on the beam dumps. High-Luminosity (HL) LHC is a planned upgrade that increases the stored beam energy by another 26%. Therefore a new set of beam dumps is currently in development. These new objects are foreseen to carry over numerous characteristics of the current design. This emphasises the importance of an improved comprehension of the behavior of the beam dumps upon beam impact in order to assess their structural performance and improve their design.

Thermo-mechanical Finite Element Analyses have previously been performed on the currently operational beam dumps to characterize their behaviour upon beam impact. The beam dumps experience a dynamic response due to the significant thermal loads due to the energy deposited by the particle beams. The almost adiabatic temperature increase in the vessel excites the vibrational modes of the devices due to their sudden thermal expansion. Up until now, however, the model showed limited ability to reproduce the displacements measured by the sensors installed on the devices. Furthermore, it does not include the support frame which can potentially influence the simulated vibrational response. Therefore, the reliability of these models has not yet been fully validated. Therefore, they cannot be used for detailed stress analyses.

This thesis describes the development of an improved Finite Element model of the beam dumps that includes their support frames. The aim is to simulate the behaviour of the devices more accurately and to create a base for detailed stress analyses. Its validity is shown by benchmarking the simulation results with available vibrational measurement data for the operational beam dumps.

The developed model compares significantly better with measurement data. This forms a validation of the developed model and the methodology of simulation, increasing security in future design and development. Furthermore, this model can be used to perform detailed sub-analysis of the support frame and its cables. This is of significant use for the design and development of the new generation of LHC beam dumps.

Preface

This is an 8th semester bachelor thesis by Jules Braken in Automotive Engineering at the Hogeschool van Arnhem en Nijmegen in collaboration with the European Organisation for Nuclear Research (CERN). Although the correlation between Automotive Engineering and the described thesis project may not immediately be apparent, various applied methods and simulation tools show close resemblance to those used in the automotive sector. The explicit solver that is used in this work (LS-DYNA) is the main tool for a wide range of OEM car manufacturers for the analysis of vehicle crashworthiness.

Reading Guide

It is expected that the reader has a general knowledge in structural engineering and the application of Finite Element Analysis. Citations are made according to the IEEE citation method. Figures without citations are created by the author for the project.
Initially, the engineering problem is defined highlighting its challenges and implications for future work. The following chapters describe CERN and the function and construction of its beam dump devices. This is followed the fundamental principles of the adopted Finite Element technology. Hereafter a clarification of the functioning of the newly developed and improved FEM model is given and finally, a discussion of the results is followed by the conclusion of the work. Numerous recommendations for further research are provided. Details concerning the analysis setup can be found in the appendix.

Acknowledgements

I would like to express my gratitude for the TDE development team at CERN and particularly to Asbjørn Lassen Lund and Nicola Solieri for their patience and guidance. Additionally, I would like to thank Jaap Janssens from HAN University of Applied Sciences for his guidance during this thesis and during my studies.

Acronyms

LIST OF ACRONYMS

CERN	European Organisation for Nuclear Research
CFL	Courant Friedrichs Lewy
CoG	Center of Gravity
CTE	Coefficient of Thermal Expansion
DR	Dynamic Relaxation
DS	Downstream
FEA	Finite Element Analysis
FEM	Finite Element Method
FLUKA	Fluktuierende Kaskade
HD	High Density
HL-LHC	High Luminosity - Large Hadron Collider
HL-TDE	High Luminosity - Target Dump External
LD	Low Density
LDV	Laser Doppler Vibrometer
LINAC	Linear Accelerator
LHC	Large Hadron Collider
PS	Proton Synchrotron
R.o.T	Rate of Twist
SPS	Super Proton Synchrotron
TDE	Target Dump External
US	Upstream

Contents

Chapter

1 Introduction

The Large Hadron Collider accelerates proton beams to velocities that reach 99.9999991% the speed of light to conduct fundamental high energy physics research [8]. When fully accelerated, each counter-rotating particle beam stores 539 MJ of kinetic energy [22]. The Target Dump Externals (TDE) are responsible for the safe absorption of the particle beam in all possible scenarios, including instances of abnormal machine operation [21]. The beam dumps consist of a 700 mm-diameter, 8.5 m-long, duplex-stainless-steel vessel that encases a core of carbon-based materials of varying densities that are selected in order to progressively absorb the energy of the particle beam [22]. An internal nitrogen atmosphere is maintained slightly above atmospheric pressure to prevent oxidation of the core materials [6].

The velocity at which the particle beams are accelerated and the quantity of protons per particle beam increase with each operational run of the LHC, leading to a corresponding growth in the total stored energy. The beam energy levels of the LHC are set to be increased by 2028 with the forthcoming High-Luminosity (HL) upgrade as clarified in table 1.1 [22].

	Run 1 (2009-2013)	Run 2 (2015-2018)	Run 3 (2022-2024)	HL-LHC (2028-)
E_{Beam}[MJ]	150	320	539	680

Table 1.1: The total beam energy to be absorbed by the TDEs in each run of the Large Hadron Collider [22].

As the current beam dumps were originally designed to withstand the beam energy levels occurring in Run 1, its design will have to be adapted to cope with the increase in required energy absorption in the High-Luminosity operation. Consequently, a new set of beam dumps is currently in development that can ensure the functioning of the upgraded collider [6].
During operation in Run 2 multiple issues were observed for the beam dumps [21]:

- The devices showed nitrogen leaks.
- The devices had moved with respect to the installed position.
- Multiple fasteners between the support frame and the cavern floor had loosened.

These findings indicated that the dynamic behaviour of the dumps was more violent than what had been anticipated [21]. Due to the deposition of up to 5% of the incoming beam energy into the stainless-steel vessel, the beam dumps exhibit a highly dynamic behaviour upon beam impact. Within 86 μs the almost adiabatic temperature increase in the vessel causes the vessel to thermally expand rapidly, exciting vibrational modes [6]. Since the discovery of this dynamic behaviour, the vibrations of the devices in operation are monitored by sensors and can be used to verify simulation results[21]. After the initial dynamic motion, the beam dumps undergo a quasi-static expansion due to the heat diffusing from the core to the vessel, and eventually transferring to the air through a cooling system [21].

Upon the discovery of the dynamic behaviour of the beam dumps, a dynamic model had to be developed to investigate the characteristics of their movement upon beam impact. This exercise had to be performed in a limited time frame. The models resulted in only a limited correspondence with measurement data of the vibrational behaviour measured at the front end of the installed devices. Table 1.2 shows the simulation results of the resulting longitudinal velocity of Run 2 beam dumps in dynamic vibration compared to available measurement data for a 110.4MJ beam dump. It describes the characteristics of the measured and simulated vibrations at the front end of the dump.

	Measurement data	Simulation	Deviation
Frequency	200 Hz	196 Hz	2%
Amplitude	0.35 m/s	1.10 m/s	214%

Table 1.2: Comparison of the frequency and amplitude of the simulated and measured longitudinal velocity of the Run 2 TDE during a 110.4 MJ beam dump[21].

As noted in table 1.2, the simulation of the run 2 TDE accurately describes the frequency of the longitudinal vibrations. However, it vastly overestimates its amplitude.

The currently installed beam dumps in Run 3 are upgraded spares of the originally designed beam dumps for Run 1. The required energy rise in High Luminosity can pose a challenge to the structural integrity of the new beam intercepting devices with potentially marginal safety factors [6]. This problem increases the stringency to generate accurate simulation results.
In the design and development phase for the HL-beam dumps it is essential to posses and use an accurate and complete finite element model of the TDE. The results of the previously created model shown in the table above will act as a reference for the comparison of the newly developed model.

Chapter

2 Engineering problem definition

The Run 3 beam dump design consists of two individual structures shown in figure 2.1. This design principle also forms the baseline for the next generation of beam dumps. These two structures are:

- The beam dump block:
  This part of the structure comprises the cylindrical vessel and its internal core made of carbon-based materials. The dump block absorbs approximately 80% of the stored beam energy [15].
- The support structure:
  The structural frame supports the weight of the dump block by two cables that are connected to the support frame and led through cable guides that are welded to the dump block. This allows the dump block to expand and contract relative to the support frame during beam impact, without allowing permanent movement of the dump block and without inducing high stresses due to over-constraining the structure [22].

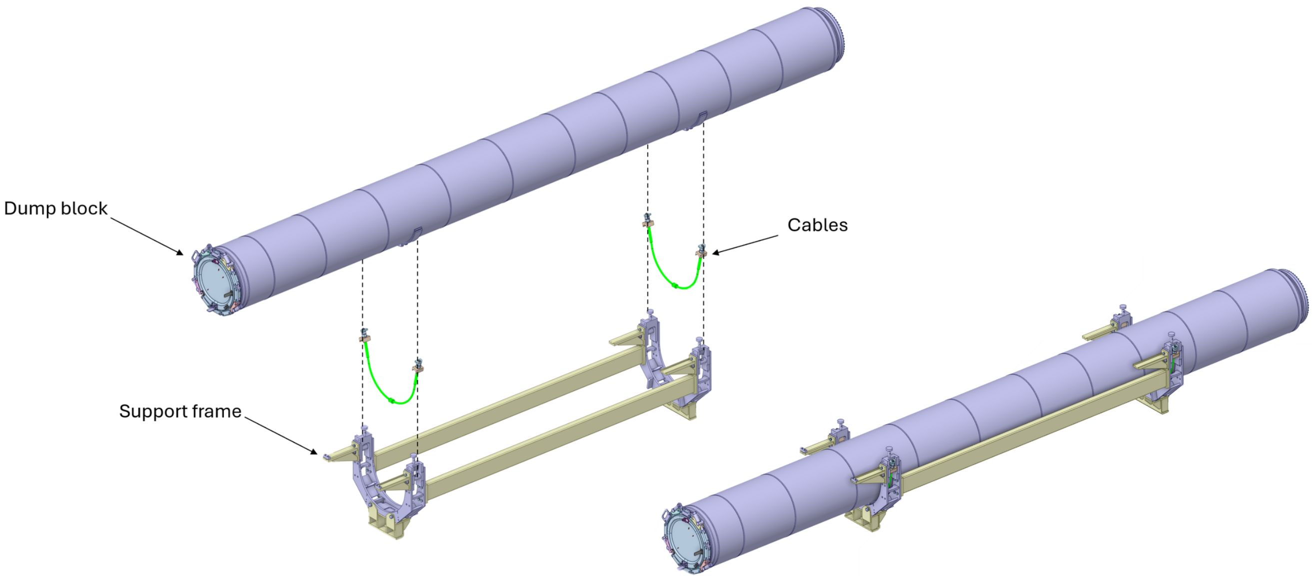

Figure 2.1: View of the beam dump construction. Left: Dump block separated from the support frame and cables. Right: The dump block installed on the cables and the cables connected to the support frame.

Finite element models for the dump block of the Run 3 beam dumps have been developed in past years to perform detailed sub-analyses or investigating potential design options. However, a comprehensive model had not yet been developed to benchmark the simulations with the sensor measurements and verify its accuracy.

The behaviour of the dump block is coupled with the support frame and its cables, that introduce reaction forces onto the vessel upon vibration. The support frame and its proprietary interactions with the dump block have not yet been incorporated in simulations. The implementation of the support structure in the model will facilitate the following assessments in future work:

- **Run 3 Operational beam dumps** (currently installed in the LHC)
  - The simulation of the currently operational beam dumps in order to clarify potential operational limits.
- **High-Luminosity beam dumps** (under development and to be installed in 2028)
  - The use of the model to simulate High Luminosity (Run 4) conditions as a crucial element in the research and development of the new beam dumps to be installed in 2028.
  - The capability of performing sub-model analyses of the support frame to conduct detailed stress - and fatigue analyses for its structure and welds.
  - The selection of cables for the High Luminosity beam dumps.

To allow these assessments an upgraded model must be developed for the currently installed Run 3 operational beam dumps that:

- Includes the support structure of the beam dumps.
- Compares well with measurement data to validate its accuracy.

The problem and objective lead to the following main research question:

Research question:

How can the support system of the currently operational beam dumps be included in finite element analysis to ensure better correlation with vibrational measurement data?

Chapter

3 The European Organisation for Nuclear Research

The European Organisation for Nuclear Research (CERN) is a research organisation in the field of particle physics. At CERN the basic constituents of matter called fundamental particles are studied [30]. In order to investigate these principles, particle accelerators are utilized to accelerate proton beams. These are ordered in proton bunches to form the complete particle beam. Figure 3.1 displays the entire accelerator complex located at CERN. The particle beam is progressively accelerated from LINAC 4 into the PS-Booster and PS to be propelled into SPS and eventually reach the LHC [30].

The LHC is a circular accelerator with a circumference of 27 km and is situated 100 m below the surface [8]. Two counter-rotating proton beams are injected into the LHC and are accelerated to 99.9999991% of the speed of light using strong electric fields [30]. Superconducting magnets ensure that the beams follow the circular trajectory around the LHC [30].

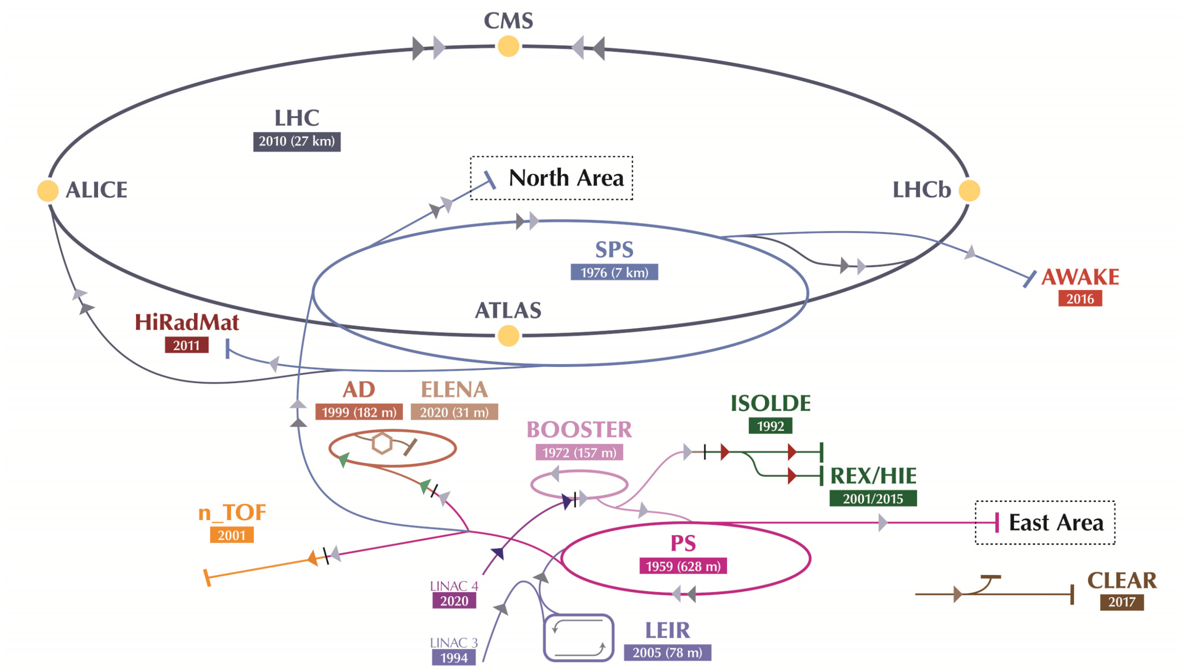

Figure 3.1: Overview of the CERN accelerator complex. the particle beam is accelerated by LINAC 4 into numerous circular accelerators (PS-Booster,PS and SPS) to eventually reach LHC [30].

The counter-rotating beams are collided within experimental detectors such as the Compact Muon Solenoid (CMS) as displayed in figure 3.2. During these collision, secondary particles are created and scattered around within a detector. The detectors gather data such as energy levels, electric charge, and the mass of the secondary particles. The produced secondary particles can be tracked, counted, and characterised to reconstruct the collision in detail [8].

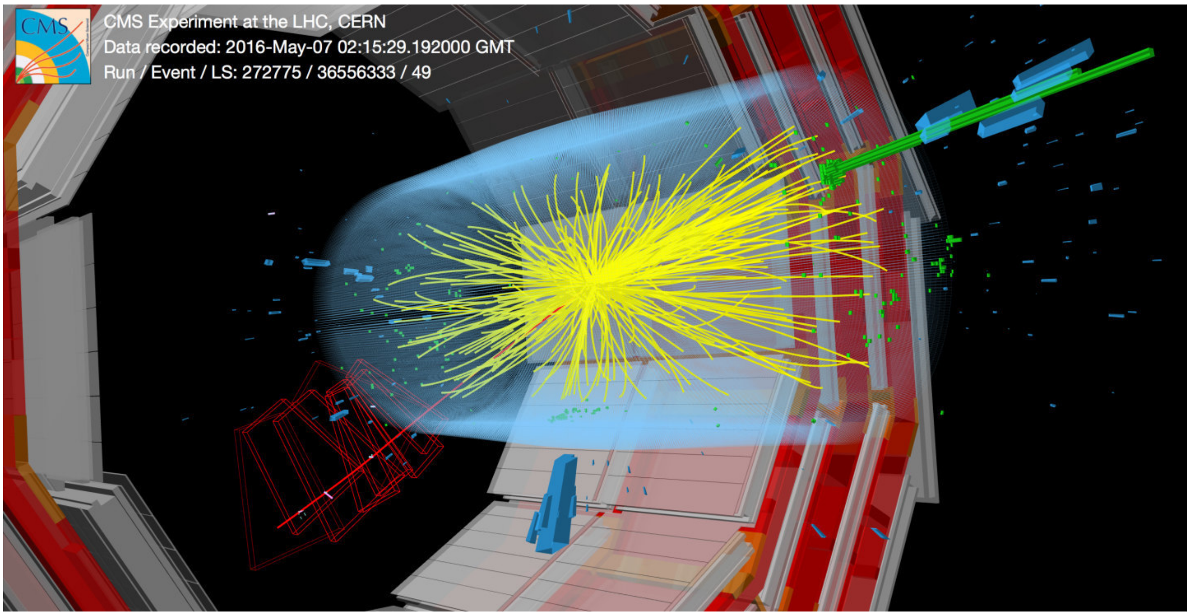

Figure 3.2: Visual representation of the scattered secondary particle paths within the CMS detector [9]

The beam energy (E_{beam}) is determined by multiplying the number of bunches (N_b) within the beam with the number of protons per bunch (I_b) and the energy per proton (E_{prot}) [22]. The beam intensity refers to the total amount of protons accelerated in each counterrotating particle beam. Table 3.1 shows the evolution of the beam energy at different generations of the LHC. The consistent increase in beam energy requires the continuous research and development program of the LHC-machine to ensure the systems' compatibility with the high energies.

	Run 1 (2009-2013)	Run 2 (2015-2018)	Run 3 (2022-2024)	HL-LHC (2028-)
E_{prot} [TeV]	4	6.5	6.8	7
N_b	1380	2556	2748	2760
$I_b[p]$	$1.7 * 10^{11}$	$1.2 * 10^{11}$	$1.8 * 10^{11}$	$2.2 * 10^{11}$
E_{beam} [MJ]	150	320	539	680

Table 3.1: Evolution in beam parameters of the LHC over various generations including the High Luminosity (HL) upgrade [22].

Due to the small size of the particles accelerated in the LHC, only a fraction of the protons collides during each revolution. As a result of the numerous collisions, the beam intensity gradually decreases [30]. Consequently, the number of collisions and the collectable amount of physics data decreases accordingly as the experiment progresses. Figure 3.3 shows a typical cycle for the LHC. Protons are injected from the SPS with a low velocity (energy) in each direction of the LHC. All particles are accelerated (ramped) to an energy of 6.5 TeV before being squeezed and adjusted in order to focus the beams and thereby increase the probability of collisions in the experiments. In the phase of stable beams for physics, the collisions take place and the intensity decreases as a consequence. At a critical threshold the beams are extracted and dumped. After this, the LHC is injected again with protons and the cycle restarts. A schematic representation of such a cycle is shown in figure 3.3.

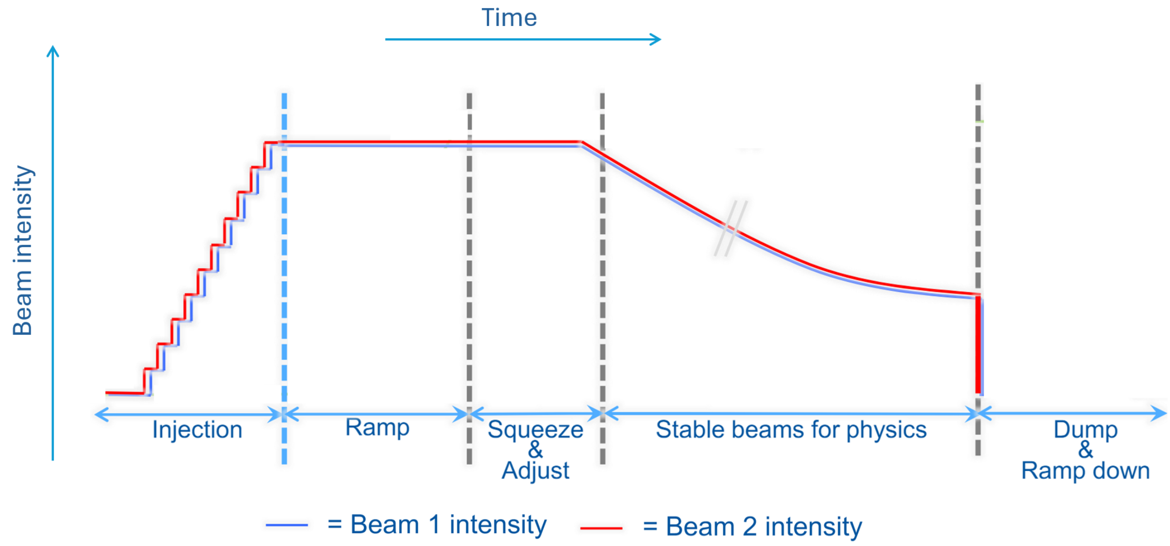

Figure 3.3: The change of the beam intensity over an LHC filling and physics cycle. The beam is dumped after reaching a critical threshold in the decrease in beam intensity created by particle collisions during many consecutive revolutions through the collider [30].

Chapter 4

The Large Hadron Collider Target Dump Externals

4.1 Procedure in the event of a beam dump

In the event of a beam dump, both particle beams are extracted by a series of electromagnetic kickers into two 600 m-long extraction lines that are positioned tangentially to the LHC ring as shown in figure 4.1 [22].

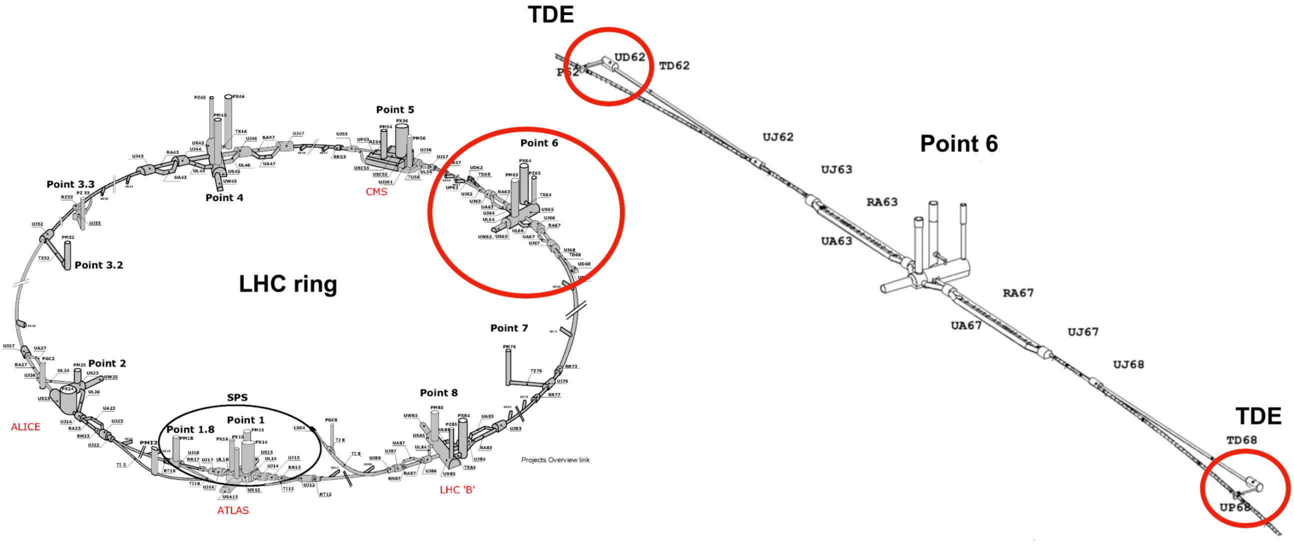

Figure 4.1: Left: Overview of the LHC accelerator ring with emphasis on point 6, where the dumps are located, indicated in red. Right: The extraction lines at point 6 are brought into close-up. In the event of a beam dump, the beam is extracted into these extraction lines and dumped in the Target Dump Externals positioned in their underground caverns(UD62 and UD68) [19].

After the extraction from the LHC, the beam is diluted by an additional set of vertical and horizontal kicker magnets [15]. This process dilutes the highly concentrated proton beam as schematically represented in figure 4.2, thereby decreasing its peak energy density when impacting the beam dumps [15]. The diluted pattern has the shape of a spiral. The corresponding distribution of energy density that is deposited in the core at the cross section where the maximum occurs can be seen in figure 4.2.

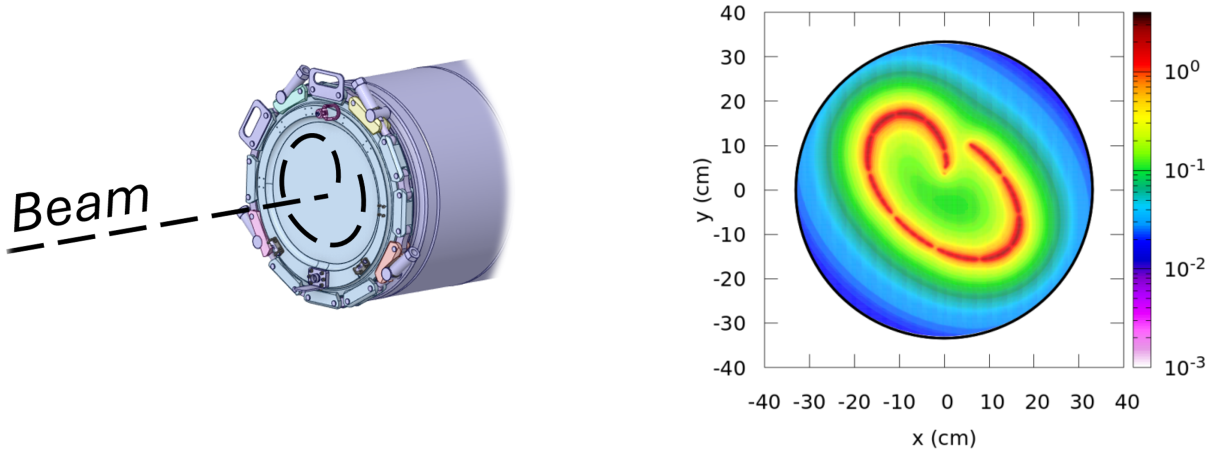

Figure 4.2: Left : The particle beam is transversely diluted by horizontal and vertical kicker magnets to decrease local energy densities. Right: Transverse energy density distribution in kJ/g along the diluted beam sweep for Run 3 beam parameters at 270cm of longitudinal depth into the dump core [15].

In typical conditions the beam dumps are subjected to lower beam intensities compared to the maximum intensity available in the LHC. This is a consequence of the beams being dumped at a reduced intensity due to a prolonged period of collisions in the physics experiments . However, the beam dumps must be able to withstand the maximum intensity of the LHC as the devices are used as essential safety equipment. This means that the beam can be dumped at any intensity from the LHC in case of abnormal behaviour of the accelerator. Therefore, the beam dumps are designed to withstand repeatedly occurring dumps when the beams have a stored energy of 539 MJ, which corresponds to the maximum energy that the LHC is capable of handling in Run 3 [22].

4.2 Function and construction of the Target Dump External

Figure 4.3 shows one of the beam dumps inside of its cavern. The dump block resting on its support frame is installed inside an iron shielding that ensures the shielding against radiation from the activated beam dumps. The dumps are cooled by air fed through cooling pipes that send air to circulate within the space of the shielding [22]. The surrounding shielding material geometrically limits the dimensional design freedom in the development phase of the HL beam dump.

Figure 4.3: One of the beam dumps installed in its underground cavern inside the iron shielding. The circular front face visible in this image is the upstream window upon which the beam impacts first. The cooling pipes are led into the shielding area.

4.2.1 The dump block

The dump blocks consist of a series of 12 mm thick, seamlessly forged, duplex (318LN) stainless-steel blanks that are circumferentially welded together to form the length of the dump block. Inside the vessel various carbon-based materials are selected to progressively absorb the energy from the proton beam [22]. Six high-density (HD) blocks of 0.7 m long, isostatic graphite (commercial grade SGL Sigrafine® R7330) are shrink fit inside the vessel to ensure a strong thermal contact and thereby facilitate heat extraction from the core to the vessel and finally to the cooling system. A series of 2 mm-thick expanded graphite sheets (commercial name SGL Sigraflex® L20012C) form the central low-density (LD) sector. Due to their low rigidity, the sheets cannot be shrink fitted in the vessel. The low-density sector is retained under slight longitudinal compression by two extruded graphite disks (commercial grade SGL Sigrafine® HLM). These are held in place by retaining rings that are inserted into grooves within the vessel and spot-welded around the circumference. Both ends of this vessel are closed off by titanium grade 5 windows to enclose a nitrogen pressure inside. This nitrogen pressure prevents the oxidation of the graphite core materials [6]. All separate components are shown in figure 4.4.

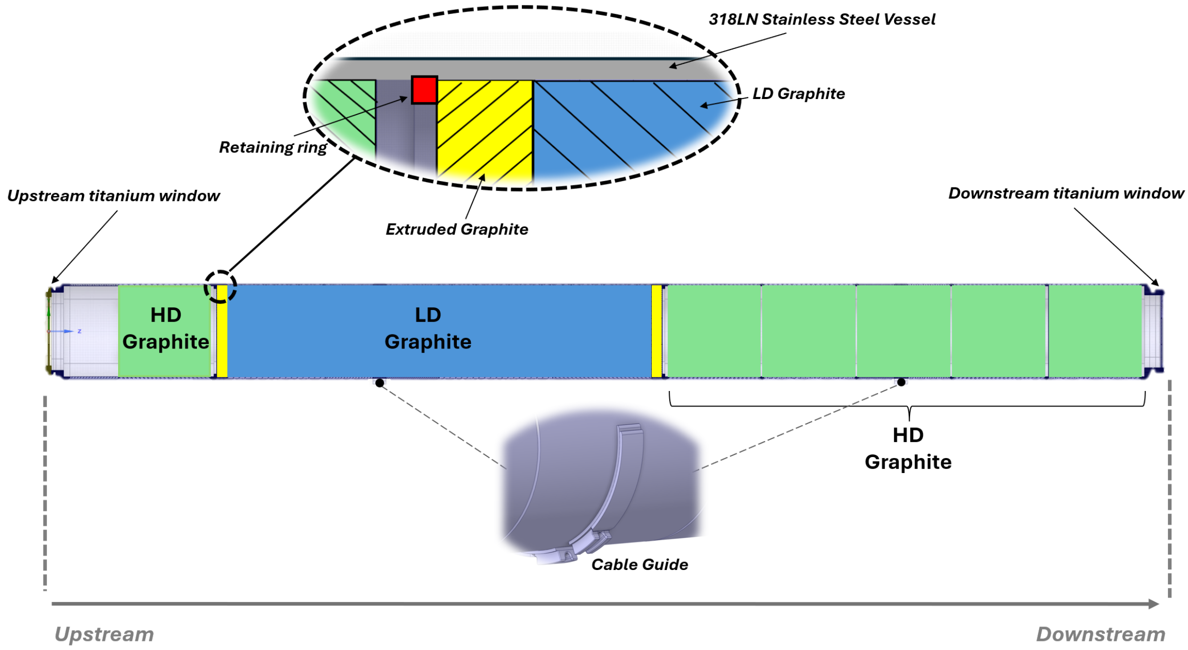

Figure 4.4: Cut view of the components and construction of the Target Dump External dump block.

In the event of a beam dump, the beam passes trough the upstream window. The protons impact the first high density graphite block and collide with its atomic nuclei [16]. The collisions create secondary particles, and a particle shower is developed through the depth of the dump that deposits the kinetic energy of the beam protons in form of heat. The development of the particle shower is controlled by the use of different densities of materials in the design of the dump core. This alteration directly impacts the probability of the occurring collisions as the probability of nuclear collisions is directly related to the material density of the impacted material [16]. Consequently, the positioning of the low-density graphite as shown in figure 4.5 limits the nuclear interactions and ensures that the low-density core is not subjected to levels of energy deposition and temperatures that it cannot withstand [22].

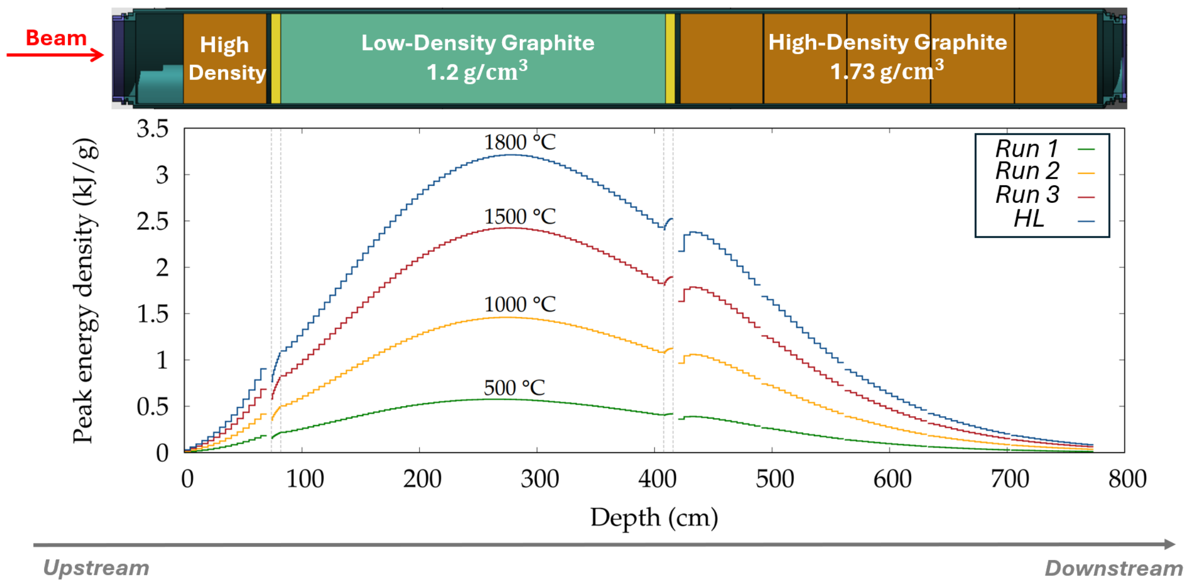

Figure 4.5: Cross-sectional view of the beam dump energy density and temperature peaks as a function of depth into the core of the beam dumps for parameters of each LHC generation [15].

The dump block absorbs approximately 82% of the total beam energy [21]. Within the dump block, the majority of the energy is absorbed by the high- and low density graphite sectors of the dump. Small fractions of the beam energy are also deposited in the windows and the vessel as indicated in table 4.1. The remaining 18% is deposited in the cast iron shielding that surrounds the dump [21].

Dump Block Component	**Material**	**Density [g/cm^3]**	**Fraction of dump block absorbed energy**
Upstream Window	Titanium grade 5	4.43	0.001%
High density graphite	SiGRAFINE®	1.73	49.5%
Low density graphite	SIGRAFLEX® Sheets	1.20	42.4%
Extruded graphite plates	SiGRAFINE® HLM	1.73	2.6%
Downstream window	Titanium grade 5	4.43	0.06%
Vessel	Stainless-Steel 318LN	7.80	5.4%

Table 4.1: Distribution of deposited energy in the components of the TDE dump block [21].

4.2.2 The support frame

The support frame as shown in figure 4.6 consists of two u-shaped S460 steel cradles that are connected by two longitudinal side members made of steel S235JR. Both on the upstream and the downstream end of the frame, a cable is transversely span across the cradle structure and bolted to a pin connection as shown in the detail view in the figure [21].

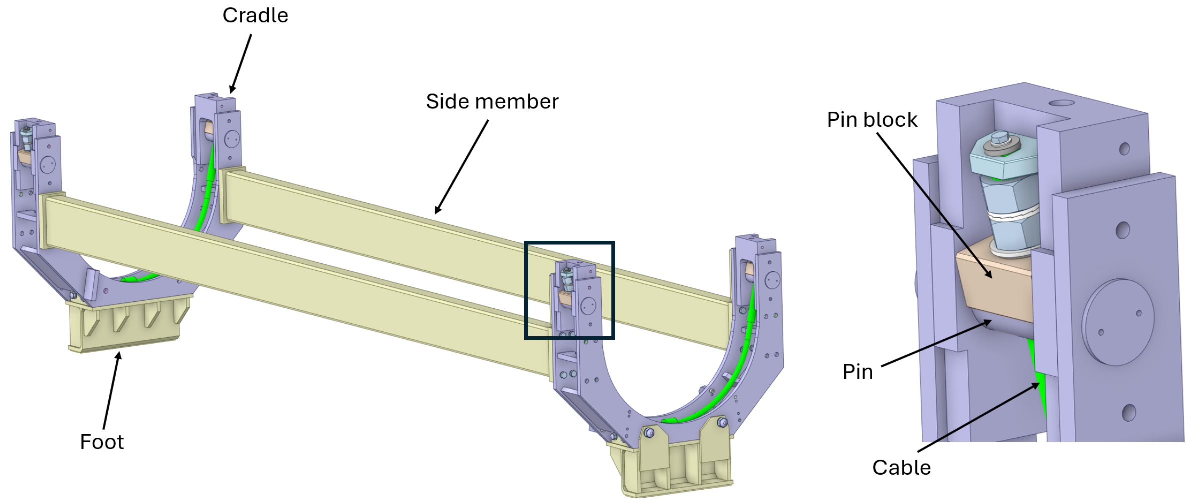

Figure 4.6: Left: The structure of the support frame with its feet, cradles and side members. Right: detail view on the cable connection.

The cables are fed through cable guides that are welded on the bottom surface of the vessel. The reason for the implementation of cables in the design of the support frame was to allow the dump block to expand and vibrate freely upon beam impact [22].

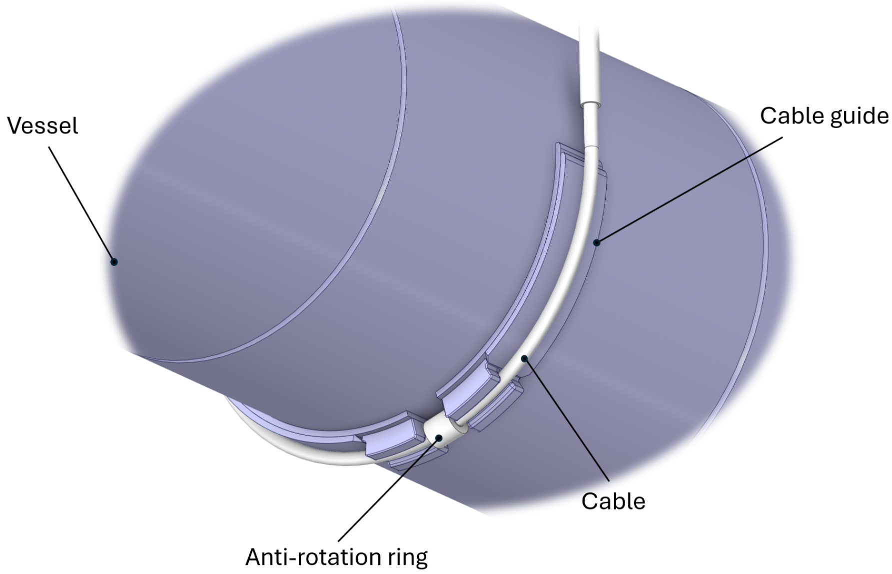

Figure 4.7: Detail view of the bottom surface of the dump block. Each cable is fed through cable guides that are welded to the vessel. An anti rotation ring prevents the ability of rotation of the vessel.

4.3 Beam dump response to beam impact

The response of the beam dumps upon beam impact can be schematically divided into two consecutive phases. An initial dynamic response occurs after the beam impact that lasts only a few tenths of a microsecond and a slower quasi-static expansion phase that can take up to 12 hours [22] as listed in table 4.2.

	Dynamic phase	Quasi-static phase
Time range	<100 ms	up to 12h

Table 4.2: Time ranges of both response phases of the TDE during a beam dump event[21].

The dynamic response of the beam dumps originates as a result of the energy that is deposited in the stainless steel. The almost instantaneous thermal expansion of the vessel leads to stress waves and strong vibrations in the device that are dampened in less than 100 ms [6]. The complete dynamic response of the dump block is the result of the excitation of its longitudinal, radial, and flexural modes of vibration. The frequencies of the different vibrational modes were verified by an eigenfrequency test on the spare dumps prior to their installation. Its results can be seen in table 4.3. Fast fourier transformation of the stress signals from the simulations at that time facilitated the identification of the most damaging modes of vibrations, at it became evident that the longitudinal mode of vibration induced the highest stresses.

Vibrational mode	Frequency [Hz]
Flexural	37
Longitudinal	200
Radial	2360

Table 4.3: Experimentally measured eigenfrequencies of three different vibrational modes of the beam dump vessel [21].

The dynamic response of the installed beam dumps are monitored with a complex suite of sensors. This includes a Laser Doppler Vibrometer (LDV). As schematically described in figure 4.8, an LDV projects a laser beam at the upstream window of the beam dump and receives the light that is reflected back. The light from a laser beam behaves like a wave with a wavelength and a frequency. When the target surface moves, it changes the frequency and phase of the scattered light [24]. This results in a phase shift of the light signal. Using the measured phase shift, the LDV calculates the velocity of the moving target surface [24]. These measurements are used as a benchmark for the simulation models at the end of this report.

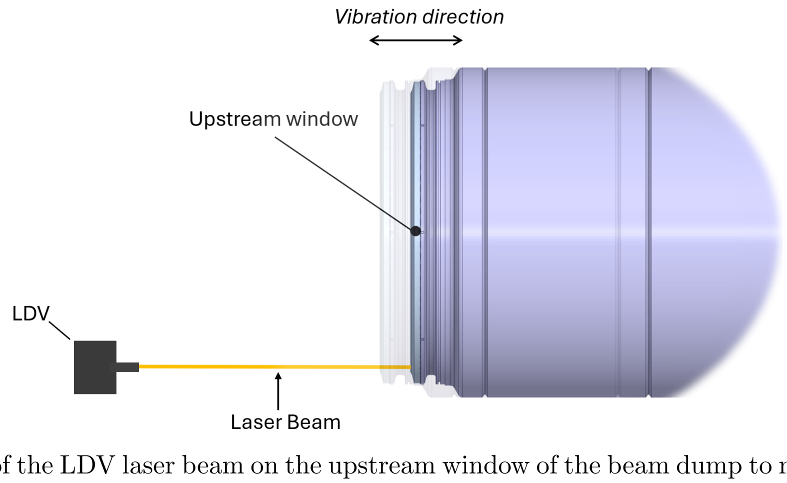

Figure 4.8: Position of the LDV laser beam on the upstream window of the beam dump to measure the magnitude and frequency of the longitudinally induced vibrations.

Chapter

5 Finite Element Method Technology

Finite Element Analysis (FEA) is often used to predict the response of components under given loads where the exact analytical solution is difficult or impossible to obtain. This difficulty can arise from complex load cases and geometries that makes an exact solution impossible. FEA is a powerful tool that allows engineers to analyse several design iterations while limiting the costs and time spent in component prototyping and testing [5].

In the Finite Element method, continuum bodies with complex geometries can be divided into a finite number of discrete elements connected by nodes. This way, the concepts of equilibrium can be applied to each element, allowing approximated solutions to be computed [13].

5.1 Finite Element Method

The behaviour of a static or steady state system can be represented as an equilibrium between internal and external forces as in formula 5.1 [13]:

$$[K] \cdot \{u\} = \{F\} \tag{5.1}$$

Where

- $[K]$ is the system's stiffness matrix
- $\{u\}$ is the displacement vector
- $\{F\}$ is the external force vector

The dynamic equilibrium equation, which is solved by the FEM in a transient analysis, expands the static formula with inertia and damping information as shown in formula 5.2 [13]:

$$[M] \cdot \{\ddot{u}\} + [C] \cdot \{\dot{u}\} + [K] \cdot \{u\} = \{F\} \tag{5.2}$$

Where

- $[M]$ is the system's mass matrix
- $[C]$ is the system's damping matrix
- $\{\ddot{u}\}$ is the system's acceleration vector
- $\{\dot{u}\}$ is the system's velocity vector

The aim of a Finite Element Analysis is to compute the displacement vector "$\{u\}$" using the known external forces and material parameters to establish the different matrices. Once the displacement vector is determined, material stresses can be computed by utilising the material strain that results from the determined displacements [13].

As mentioned, the geometry of an object is discretised into a number of finite elements. The stiffness matrix of the system can be determined by summing the stiffness matrices of the individual elements as indicated in formula 5.3. The stiffness of an element can be determined with the integral mentioned in formula 5.4 [20]:

$$[K] = \sum_{n=1}^{n_e} [k_e] \tag{5.3}$$

$$[k_e] = \int_{V_e} [B^T] \cdot [E] \cdot [B] dV \tag{5.4}$$

Where

- n_e is the number of elements of a given structure
- $n = 1$ denotes the first element involved in the sum of all stifness matrices
- $[k_e]$ is the stiffness matrix for the element
- $[B]$ is the conversion matrix describing the relations between displacements and strains
- $[E]$ is the constitutive matrix describing the relations between stresses and strains
- V_e is the element volume

Shape functions are polynomial functions that describe the displacement along every point within an element under applied loads [13]. Linear elements use linear shape functions, which means the displacement field within the element is interpolated using linear polynomials. This generally limits necessary computational power during calculation. However, its accuracy is generally lower than reached with the use of higher order polynomials [20].
Consequently, quadratic elements use quadratic shape functions, which means the displacement field is interpolated using quadratic polynomials. They show higher accuracy in results, but posses the drawback of requiring more computational power [20].

Integration points are used to evaluate field variables (such and stress and strain) within each element using the gradient of the shape functions. Full integration elements ensure high precision by using multiple integration points along an element to calculate element strains. Reduced integration elements only assess the element strain in a single point of the element. This reduces computational cost but can compromise in result accuracy [1].

5.2 Time integration schemes

In structural mechanics, static and dynamic problems can be distinguished by the level of induced strain rate. Based on the applied strain rates of the engineering case, different time integration schemes are used in order to appropriately compute its results. A time integration scheme is a method used to approximate the solution of time-dependent problems over a sequence of discrete time steps. For the purpose of thermo-mechanical analyses, two distinct classes of methods are used depending on the application of the component to be analysed [4]. These are the implicit and explicit time integration schemes as exhibited in the examples in the following image.

Implicit algorithms are generally used in static or quasi-static simulation efforts, whereas the explicit method is more appropriate in dynamic cases with high introduced strain rates [4] such as the dynamic response of the beam dumps.

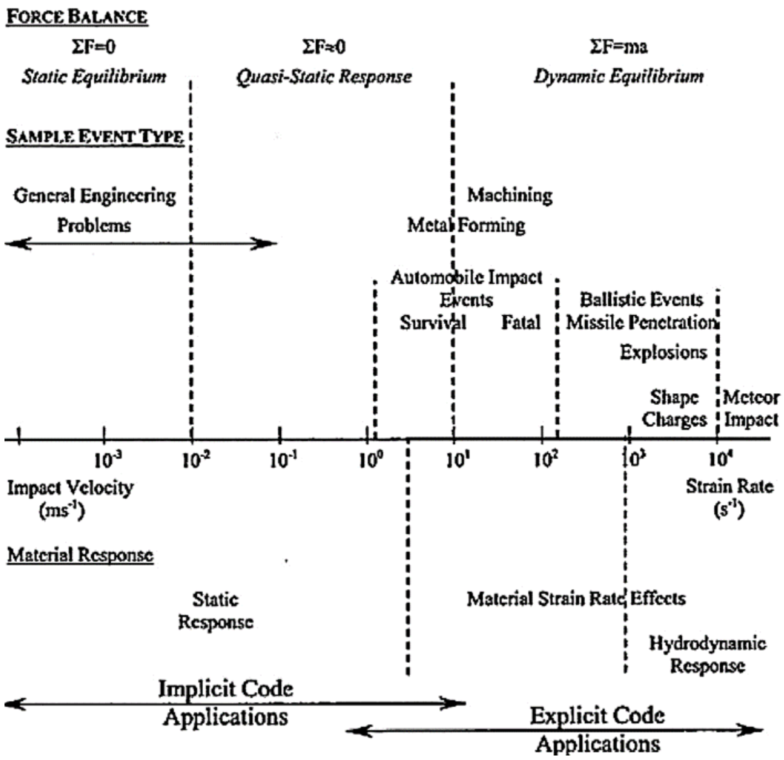

Figure 5.1: General applications of implicit and explicit time integration schemes in finite element analysis [19]

5.2.1 Implicit time integration

Implicit analysis is commonly used in the analysis of static or quasi-static behaviour of a system. In implicit analysis, typically full integration elements are utilised, leading to a high level of result accuracy [4].

If the solution of nodal displacements $y(t_n)$ at time step t_n was known, the solution at $y(t_{n+1})$ for the next timestep t_{n+1} can be computed using either an implicit or explicit time integration scheme. The implicit method uses the unknown slope of time step t_{n+1} to compute the solution. This means that for implicit time integration, the solution has to be solved through a systems of equations that requires a solution process where stiffness matrices are inverted. This is computationally expensive and require substantial amounts of memory [4]. Figure 5.2 shows a visual representation of the explained implicit time integration scheme. It can be demonstrated that implicit time integration schemes are unconditionally stable, regardless of the time step size taken. In this type of time integration scheme, quadratic elements with full integration are generally used [4].

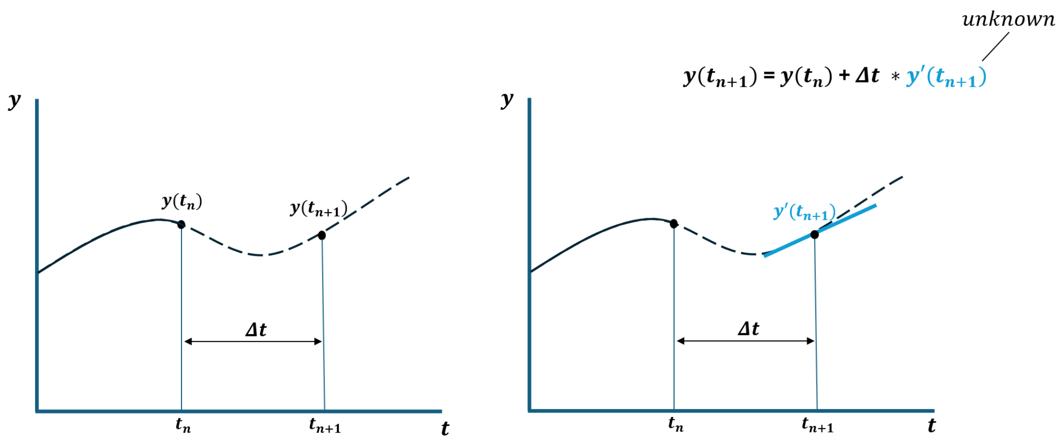

Figure 5.2: The time integration of the implicit time integration scheme shows the use of an unknown slope of a "future" time step to compute the results for y at t_{n+1}.

5.3 Explicit time integration

Using the same example as mentioned previously, the explicit method would use the known slope of time step t_n to compute the solution at timestep t_{n+1} [4]. This means that the solution can directly be extrapolated based on historic information as all values in the equation are known. No separate calculation steps for matrix inversions are necessary. This dramatically reduces the computational expense that is required to solve each timestep of the model compared to the implicit integration method. Figure 5.3 shows a visual representation of the explained implicit time integration scheme. In this type of time integration scheme, linear elements with reduced integration are generally used [4].

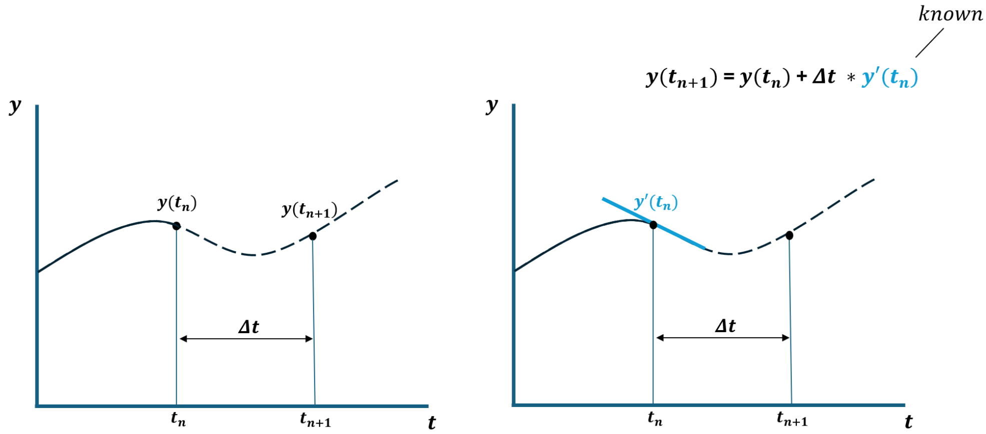

Figure 5.3: The time integration of the explicit time integration scheme shows the use of an known slope of a performed time step to compute the results for y at t_{n+1}.

Explicit time integration is conditionally stable. The stability of the model depends on the size of the timesteps that the model takes [3]. The time step size must be chosen carefully to compute stable results. The step time is limited so that stress waves are not allowed to propagate further than the characteristic length of the smallest element in a single time step. In order to apply ensure compliance with this requirement, the Courant-Friedrichs-Lewy (CFL) condition is used. The maximum time step that can be adopted for the model is described by the following equation [3]:

$$\Delta t \leq f * \left(\frac{h}{c}\right) \tag{5.5}$$

Where

- Δt is the time step size.
- f is the time step safety factor.
- h is the characteristic length of the smallest element in the model.
- c is the speed of sound in the material which is expressed by 5.6:

$$c = \sqrt{\frac{E}{\rho}} \tag{5.6}$$

Where

- E is the elastic modulus of the material.
- ρ is the material density.

From these equations it is immediately apparent that the generated mesh can have significant implications on the computational time required to solve the model. Not only does the number of nodes and elements drive up the computational expense, but in addition the amount of time steps required to solve a given time duration of the model have high sensitivity to the characteristic length of the smallest element in the model. Therefore, detailed inspection of the mesh must be performed prior to the submission of the job in order to ensure the implementation of a satisfying mesh both from the thermomechanical point of view and from a computational aspect.

Due to the dynamic response of the beam dumps upon beam impact, an explicit time integration scheme is adopted for the development of the model which uses linear elements with reduced integration.
A summary of the characteristics of both implicit and explicit time integration is seen in table 5.1.

	Implicit Analysis	Explicit Analysis
Analysis application	Quasi (Static)	Dynamic
Stability	Unconditionally	Dependent on CFL time step
Element type	Quadratic	Linear
Integration	Full integration	Reduced integration
Memory use	Relatively high	Relatively Low
CPU use	Relatively low	Relatively high

Table 5.1: Characteristics of implicit and explicit time integration schemes.

5.4 Computing of thermal loads

The FLUKA Code, developed at CERN, is a versatile Monte Carlo code used for calculating particle transport and their interactions with matter. Its primary objective is to incorporate the most accurate physics models to simulate particle interactions with matter. The code has undergone numerous benchmark studies against experimental data, aiming to enhance its reliability [7, 25].

As particles move through matter, they undergo various radiation-matter interaction processes, resulting in:

- Changes in direction (movement of target atoms)
- Loss of energy (transfer of energy to the material, causing heating)
- Creation of additional particles (development of a radiation or particle shower)
- Formation of residual nuclei, which may be radioactive (release of immediate or delayed radiation).

For a detailed understanding of nuclear interaction mechanisms, a more detailed description can be found in figure 5.5 but is beyond the scope of this thesis. The mechanisms depicted on the particle tracks in this figure are included in the code and are influenced by physics phenomena and associated probability distributions [25].

For the beam dumps the FLUKA simulations use beam parameters, component geometry, and the material properties of the dumps. In the context of this project, the code outputs an energy deposition map, which is essentially a mesh consisting of bins where each bin describes the energy deposition in that given volume. The energy deposition is generated an supplied by a seperate physics section within CERN.

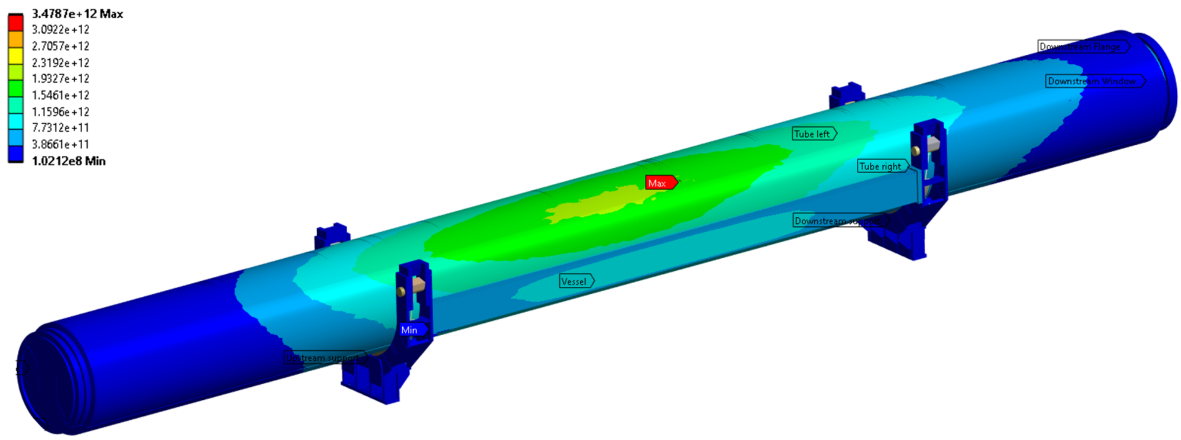

Figure 5.4: Visual representation of the energy density deposition in [W/m^3] of the Run 3 beam dump for a 402.1 MJ dump.

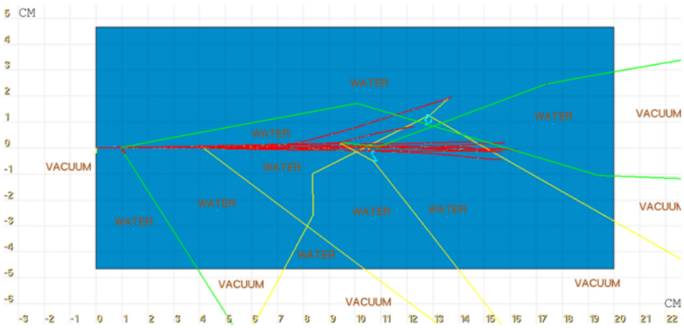

(a) 10 primary 150 MeV protons in H_2O

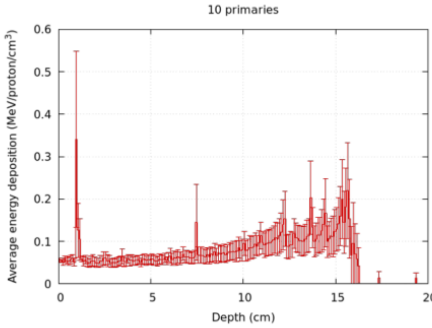

(b) Average energy deposition as a function of depth with uncertainty indicators

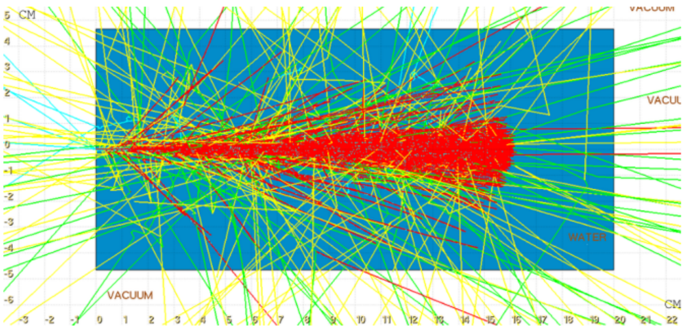

(c) 1 000 primary 150 MeV protons in H_2O

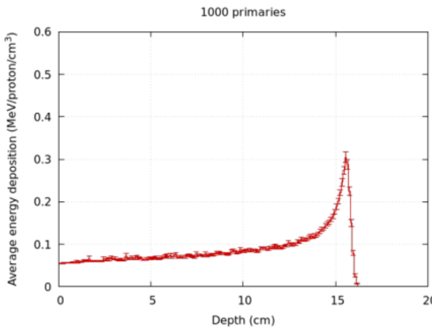

(d) Average energy deposition as a function of depth with uncertainty indicators

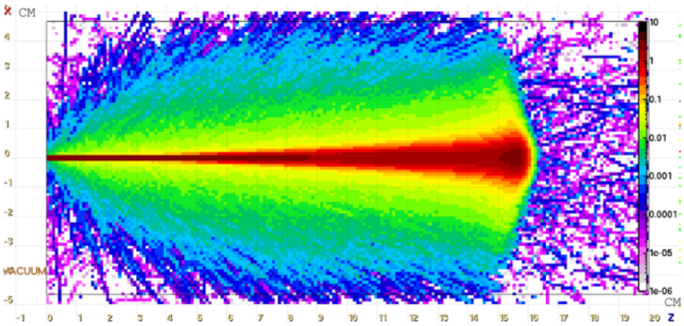

(e) 100 000 primary 150 MeV protons in H_2O. Proton tracks replaced by distribution

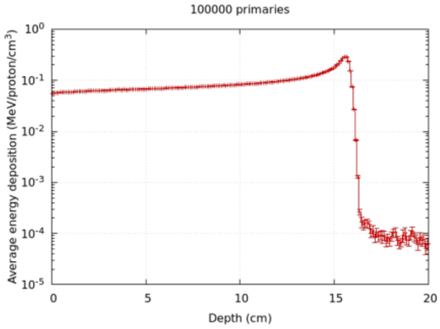

(f) Average energy deposition as a function of depth with uncertainty indicators. Logarithmic scale

Figure 5.5: Along the evolution of the images depicted above, an increasing number of results for 150 Mev protons impacting water is shown. The more iterations of interactions are simulated, the further the uncertainty decreases in the obtained results [19, 25].

5.5 Conclusion and aims

It has been clarified that the the beam dumps behave dynamically upon beam impact. For this reason, explicit time integration using linear elements with reduced integration must be used in order to develop a model that are able to replicate the dynamic phenomenon. Due to the use of explicit time integration scheme, it is essential to pay close attention to the element size and quality for the developed model, as this may have a significant effect on computational time.

Chapter

6 Run 3 beam dump finite element model

Finite element models for the dump block of the Run 3 beam dumps have been developed in past years to perform detailed sub-analyses or investigating potential design options. However, a comprehensive model had not yet been developed to benchmark the simulations with the sensor measurements and verify their accuracy. Therefore, a new finite element model must be developed and validated to form a reliable foundation for modelling future designs and performing sub-analyses of the support frame.
The diagram below shows a fundamental overview of the workflow for the development of the model.

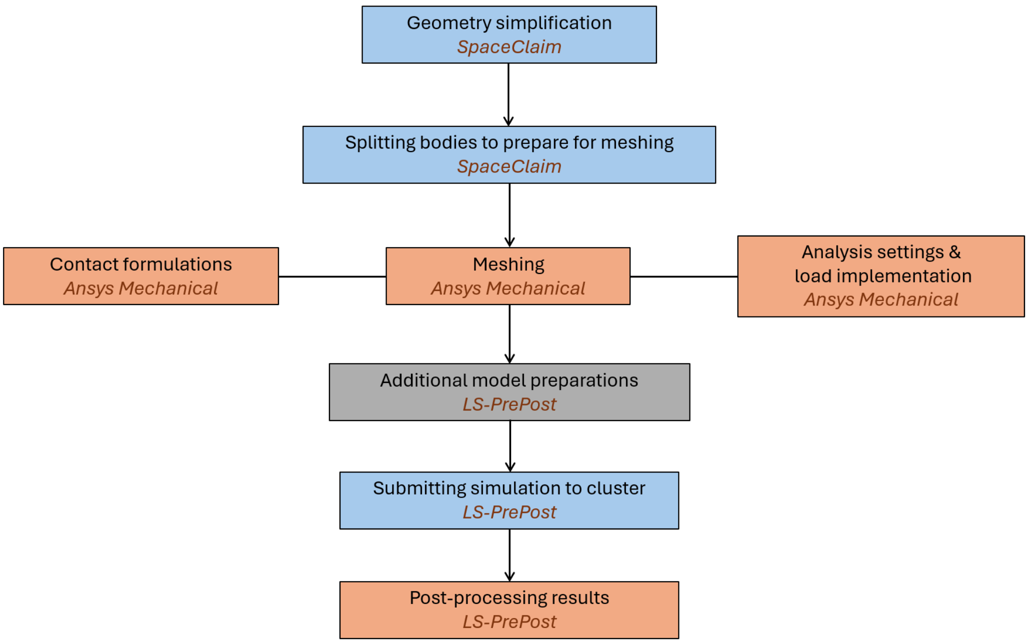

Figure 6.1: Basic overview of the seperate steps undertaken to realise a fully functioning finite element model of the beam dumps. Additionally, the used tools are mentioned with which the specific steps are undertaken

Firstly, the entire geometry is simplified and prepared before a mesh is applied. Contacts, boundary conditions and the thermal loads are implemented accordingly. Special attention is paid to adequately model the cables and developing an appropriate range of steps within the analysis for the application of gravity and the establishment of contacts. Lastly, the simulation is submitted and run on a cluster and its results are retrieved and analysed to compare to measurement data.

6.1 Model geometry and mesh

To develop an accurate and efficient model the geometry of the beam dump is carefully discretised while taking element quality and size into account. Firstly, the original geometry has been simplified. All bodies have been split into simpler geometries to support the meshing algorithm in its discretisation and to ensure the implementation of hexahedral elements. An example of such body preparation is exhibited in figure 6.2. Details on the meshing strategy and its properties are mentioned in appendix A.1.

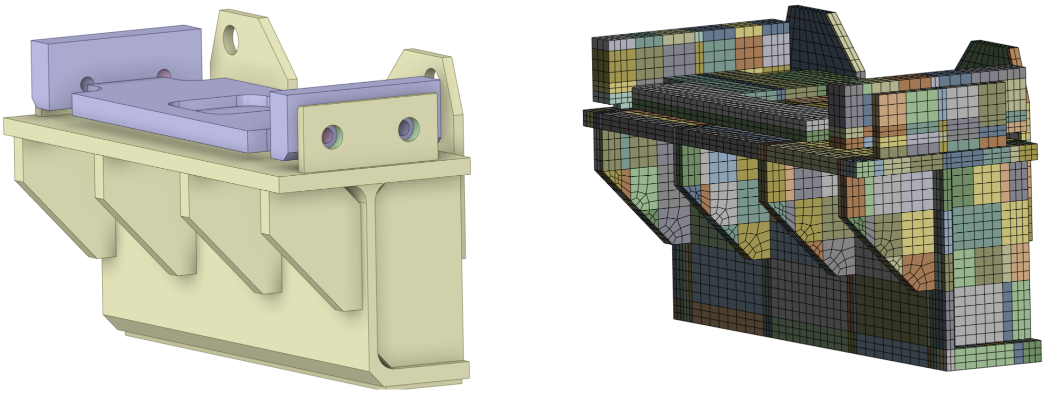

Figure 6.2: Example of simplifications, divisions and discretisation of a component of the support frame: the cradle foot

Although tetrahedron shaped elements are versatile in their use and simple to apply to many shapes, hexahedron elements have been chosen to use. Well-shaped hexahedron elements generally produce accurate results at a lower computational cost than tetrahedrons[1].

In thin-walled constructions as the beam dump vessel, shell elements could be used for its modelling. These elements assume a linear stress gradient over the thickness of the material cross section [28]. This could be a valid assumption for the model and would reduce the computational cost. However, the implementation of solid elements in the vessel increases the practical simplicity of the model setup, preventing more complex couplings between shells and solid elements. For this reason, it has been chosen to implement four elements through the thickness of the vessel to still capture flexural displacements accurately.

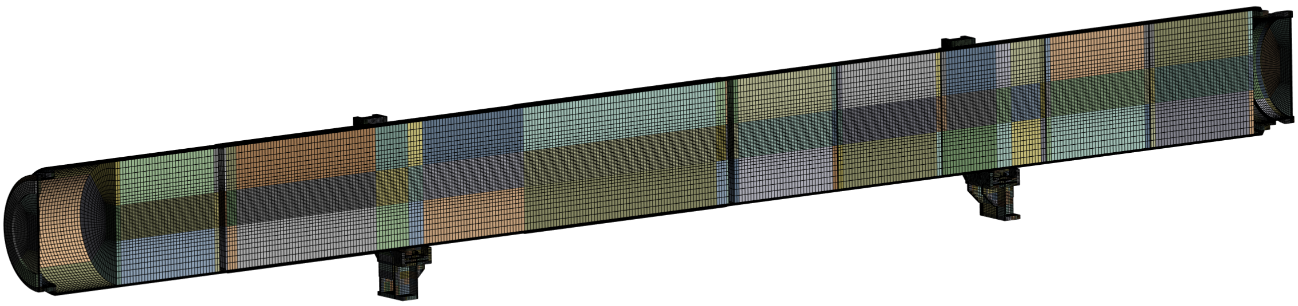

Figure 6.3: Longitudinal cross sectional view of the meshed run 3 beam dump including its support frame.

6.2 Contacts and boundary conditions

Many bodies in the model are connected by contacts. To perform the simulation accurately, these contacts must be determined to behave realistically. Details on this contact definition can be read in appendix A.2.

6.2.1 Dump block

For simplicity the welds of the vessel are not included in the model. The separate sections share the topology, which means that the various bodies in the vessel are connected by sharing the same nodes at interfaces in contact. All remaining welded and bolted sections of the dump block are connected by bonded contacts. The involved surfaces are neither allowed to separate nor slide in respect to each other, prohibiting relative motion [2].

The high-density blocks are shrink fit inside of the vessel and their contact is modelled using a special contact formulation in LS-DYNA used for interference fits (*SURFACE_TO_SURFACE_INTERFERENCE). This contact formulation is implemented using penalty stiffness. This means that the geometry is interfering at initiation of the simulation, after which the contact stiffness is ramped up until no interference between the vessel and the block is present [17].
The low-density sector is modelled with a frictional contact since it is not shrink fitted in the vessel.

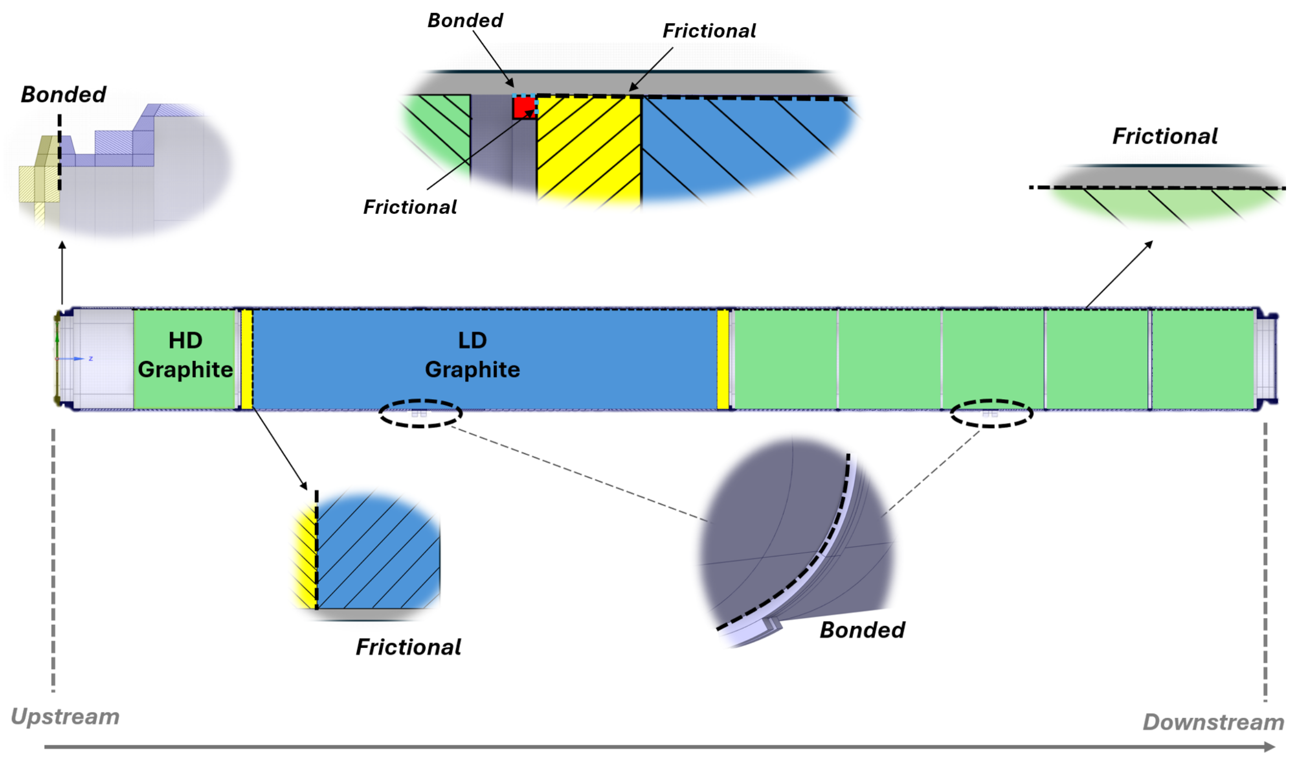

Figure 6.4: Contact definitions between surfaces of the beam dump block.

6.2.2 Support frame

The separate bodies of the support frame are mainly modelled using bonded contacts as shown in figure 6.4. Bonded contacts are applied as the bodies are either welded or strongly bolted together. The cables are connected to the cable guides on the vessel by frictional contacts. A detailed description of the contact interaction between the cables and the cable guides on the dump block is found in chapter 6.4 and appendix A.3.1.

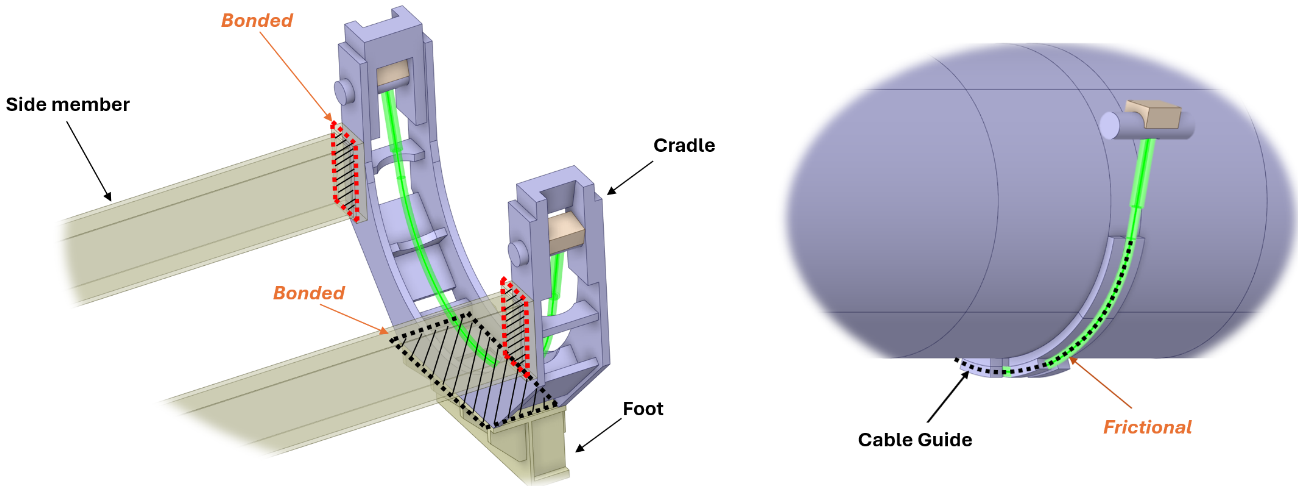

Figure 6.5: Contacts between the support system components and the vessel.

As the foot of the cradle is strongly bolted to the shielding installed in the cavern floor, this boundary is treated as a fixed support. This means that the bottom side of each foot is constrained in all directions for both translation and rotation. A bolted connection to a rigid floor could be implemented, however it would increase the complexity and calculation time of the model. As this model is not directly aimed towards performing stress analyses, the fixed support is considered as a viable option.

6.3 Modelling the support cables

Metallic wire rope is widely used in mechanical and civil engineering. They acquire their strength by combining the strength of many individual wires or fibres. They are mainly made for axial loading but specific ropes are also developed to resist a certain degree of bending and twisting. The individual strands and wires as shown in figure 6.6 come into contact when loaded and exert friction onto each other. Many configurations of helically wound cables exist on the market [14].

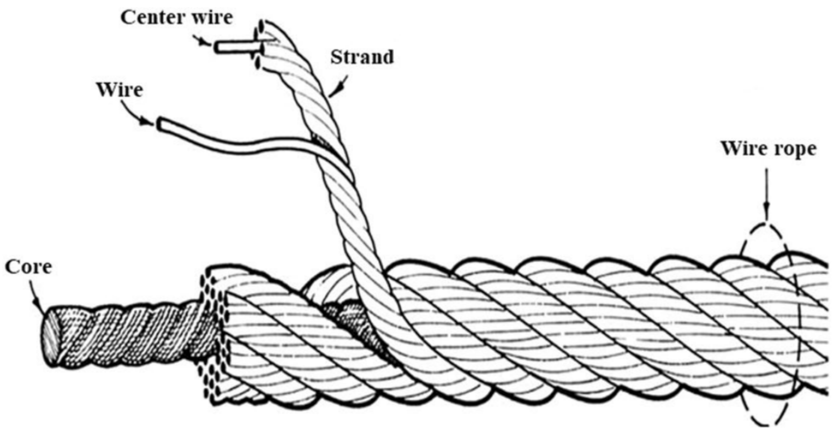

Figure 6.6: Example of the composition of a steel wire rope [14].

Knowledge of the installed beam dump cables and their out of axis properties is relatively limited. To perform a better understanding of the load case that these cables are exposed to, finite element analysis with varying cable parameters can be applied. This way the effects of varying cable parameters can be studied in a sensitivity analysis.

6.3.1 Beam elements

From a modelling perspective, it is complicated and computationally expensive to include individual strands and wires of a cable. Simplified formulations must be used to keep computational costs low [26]. Wire rope can be simulated using a beam element formulation [26]. A beam element is an element that connects two nodes. The nodes of a three-dimensional beam element each have three rotational and three linear degrees of freedom. Thus, this element can capture deformation in the form of axial, bending, and torsional motion. It generally uses Euler-Bernoulli beam theory to compute these deformations [13]. The calculated strains can be used to integrate the axial stresses over the cross-sectional area of the beam. This leads to the consequent axial forces in the cables[23].

An Euler-Bernoulli beam neglects shear deformations, implying that any cross sectional plane within the beam remains perpendicular to the neutral axis of the beam during deformation as shown in figure 6.7. Shear flexible beams such as the Belytschko beam do consider shear deformation. In that case, cross-sectional planes can rotate (with angle ϕ) in respect to the beam neutral axis upon the application of a shear load as visible in figure 6.7. This makes use of the Euler-Bernoulli beam adequate for long slender beams under small deformations, whereas the Belytschko beam is more accurate in shear loading for shorter beams under larger deformations. [23].

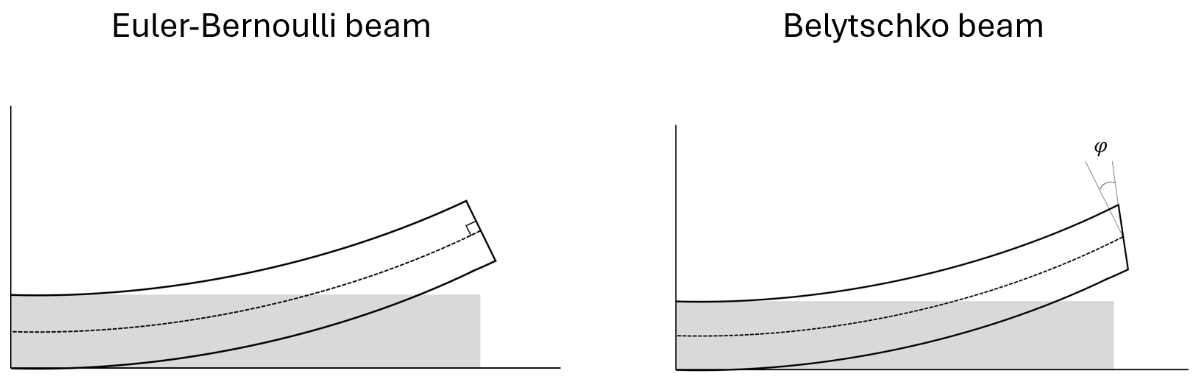

Figure 6.7: Left: deformation principle of an Euler-Bernoulli beam; cross sectional planes remain perpendicular during deformation, shear deformation is not accounted for. Right: deformation principle of a Belytschko beam; cross sectional planes can rotate in respect to the neutral axis, shear deformation is accounted for.

6.3.2 Beam element type and material assignment

The LHC-beam dumps transversely exert their weight onto their supporting cables. Due to the introduced effect of shear deformation, an Euler-Bernoulli beam would not describe the cables deformation accurately. Midwest Roadside Safety Facility conducted extensive testing, research, and simulation to find an optimised manner of simulating transversely loaded structural cables [26]. Their results found the simulated behaviour of the Belytscko-Schwer beam in combination with its material assignment (*MAT_MOMENT_CURVATURE_BEAM) to correspond exceptionally well with the physical testing of a metal wire rope. Its LS-DYNA model performed significantly better than any other element types by showing substantially more accurate results than multiple iterations of various types of beam elements [31]. In the mentioned study the cables were dynamically loaded transversely to their axial direction as shown in figure 6.8. This closely represents the load applied to the cables of the beam dumps.

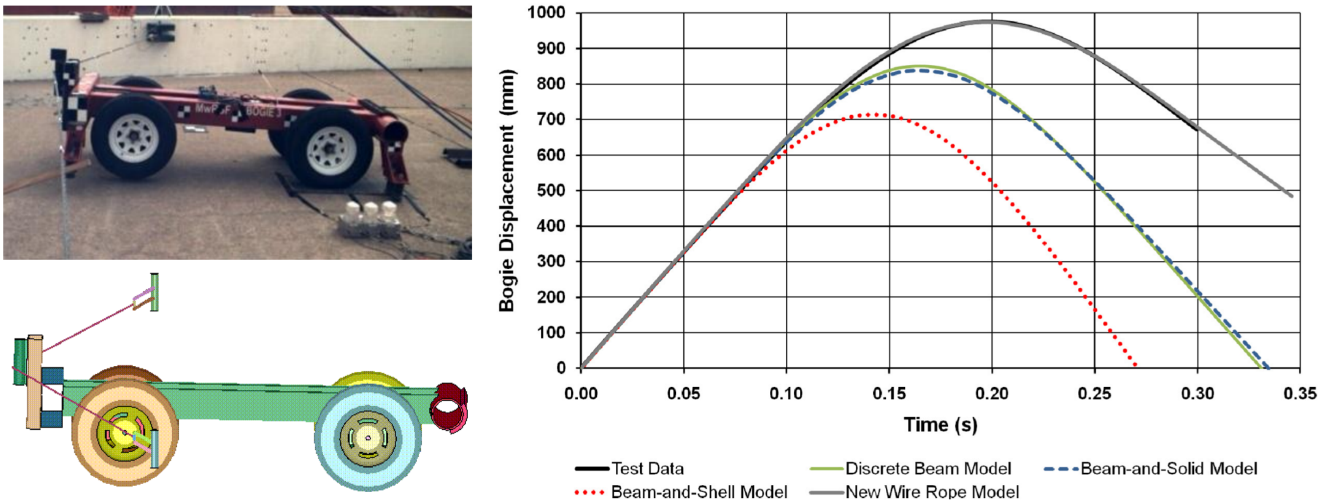

Figure 6.8: Cable testing and simulation performed by Midwest Roadside Safety Facility. Left: A bogie is propelled into a steel wire rope. Its displacement upon impact is monitored in testing and simulation. Right: Testing- and simulation results of bogie displacement. Various beam elements are applied in the simulation of the cable. "New Wire Rope Model" denotes the use of the Belytscko-Schwer beam in combination with "*MAT_MOMENT_CURVATURE_BEAM" material assignment and shows exceptional correspondance with measurement data [26].

In order to implement the beam formulation in LS-DYNA a series of material relations must be specified[31]:

- Axial strain to axial force
- Curvature to bending moment
- Rate of twist to torque

For the cables implemented in the beam dump model, the strain-force relationship is a known curve supplied by the cable manufacturer. The curvature to bending moment and rate of twist to torque curves are not to be found in datasheets and difficult to quantify since these cables are rarely manufactured for twist and curvature. However, indications of cable properties have been found on similar cables used for comparable applications. As these properties form an uncertainty in the cable model, a sensitivity study has been performed to analyse the influence of the applied properties. This sensitivity study is discussed in chapter 8.

6.3.3 Connection between cables and frame

Special attention has been paid to the connection of the cables to the pins of the support frame due to the complexity of connecting a beam element to the pin block of the support frame. In reality, the cable is connected to a blot that is fed through a hole of the pin and the pin block as shown in figure 6.9.

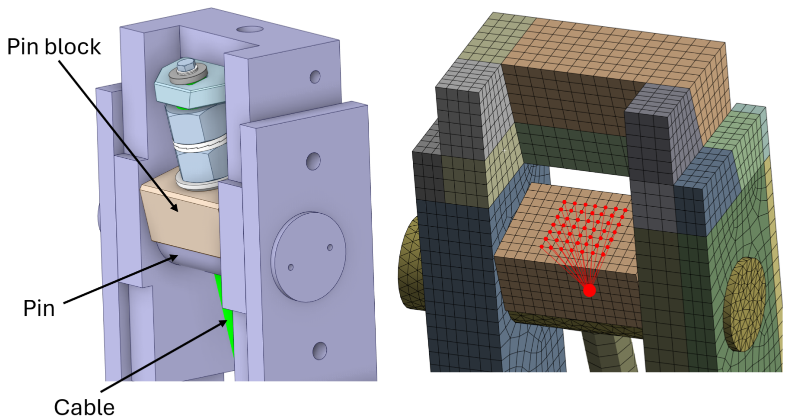

Figure 6.9: Left: complete geometry of the bolted cable connection to the support frame. Right: Adopted solution for modelling the connection of a node of the cable beam elements to the nodes of the pin block of the frame.

Multiple connections were tested to check their behaviour as shown in figure 6.10. The main three connection types considered were:

- **Rigid Springs**
  Springs with high stiffness are manually connected between the top node of the beam element and nodes on the top surface of the pin block. Consequently, these nodes are locked for relative deformation with respect to each other.
- **Node to surface contact**
  This is a penalty-based contact. In a penalty based contact a contact force is applied to resist any penetrations between multiple bodies [2].
- **Nodal rigid body constraint**
  This method is very similar to the approach of the rigid springs as the last node of the cable and a set of nodes on the surface of the pin block are selected to not move with respect to each other. However, this nodal rigid body constraint is a separate function within LS-DYNA that allows for a more practical application of the connection while modelling [17].

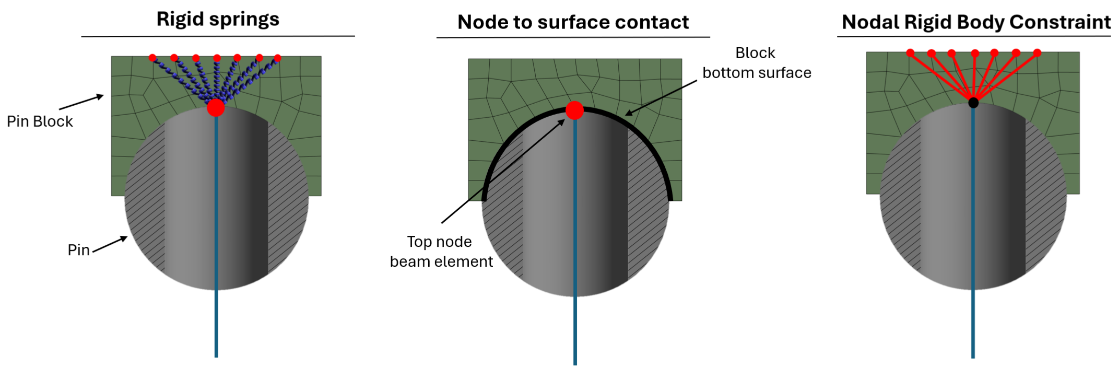

Figure 6.10: Three considered contact options between the cable and the pin block of the support frame.

In a separate analysis a sub model of these cable connections is reproduced to test the behaviour on a simplified model before selection and implementation in the global model. In the sub model shown in figure 6.11 the pin and pin block have been connected by a frictional connection. Three separate sub models are created, each implementing a different connection between the cable and the pin block. One beam without any contacts to other bodies acts as a reference beam. A displacement has been applied to the bottommost node of the beam of each type of considered contact mentioned in table 6.10. The resulting axial force in the beam of each connection type has been compared with the axial force of the reference beam. This comparison is shown in table 6.1.
If the axial forces are similar between both models, the contact is rigid and does not allow for much separation between the beam element and the pin block. The only reason for inaccuracy should occur due to local deformations of the pin.

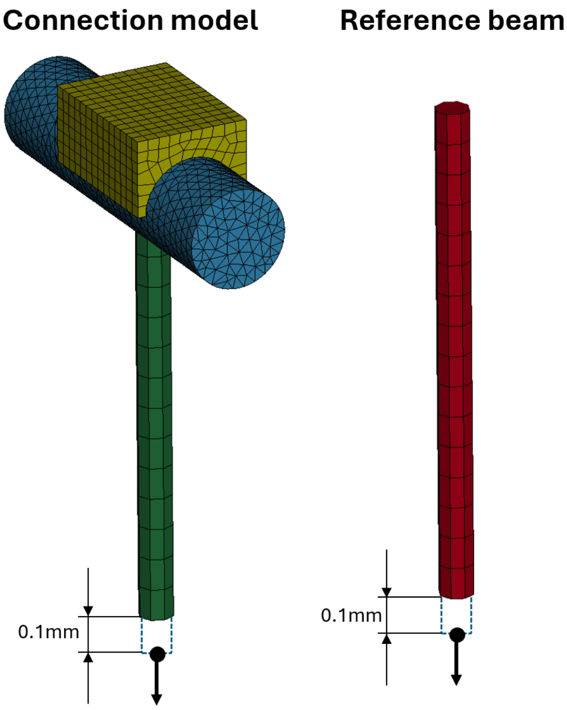

Figure 6.11: Sub model of the connection between the cables and the support frame pin blocks. Left: full sub model including the connection between the beam and the pin block. Right: beam that acts as a reference for axial force result comparison.In both cases a displacement of 0.1mm has been applied.

Table 6.1 shows that the rigid spring connection exhibits relatively accurate results as its resulting axial force approaches the resulting force in the reference beam the most closely. The nodal rigid body connection shows comparable results. However, its calculation time is significantly lower. For this reason, the nodal rigid body connection is implemented in the full model of the beam dump support structure.

Connection type	Computational time [s]	Resulting axial force [kN]	Deviation [%]
Reference beam	1	23	-
Rigid springs	160	8	9.1
Node to surface contact	20	20.9	65.2
Nodal rigid body	1	20.1	12.6

Table 6.1: Simulation results for beam element axial forces in a sub model of the cable connection and its reference beam for an analysis time of 0.001s, run locally.

In the model of the support frame the pin is connected to the support frame with a frictional contact as shown in figure 6.12. Similarly, the pin block is connected to the pin with a frictional contact. This allow the pin to rotate in the slots of the support frame and for the pin block to rotate on the pin, which is an accurate representation of their potential interaction.

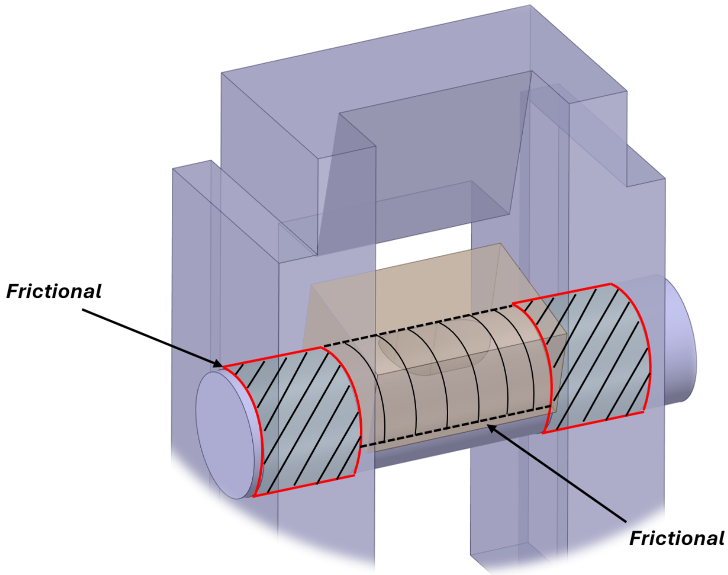

Figure 6.12: Close-up of the pin connection to the support frame highlighting its frictional contacts between the pin block, the pin, and the frame.

6.4 Dynamic Relaxation

A dynamic relaxation phase finds its use in dynamic models that must be prestressed with several static conditions before intiating a transient phase. Only this way, the main phase of the simulation can initiate in a stable manner without any significant residual disturbances caused by preloading [18].

A dynamic relaxation phase starts by ramping preloads onto a model. The induced preload leads to a dynamic oscillation in nodal displacements. These nodal velocities are damped out until a convergence factor is reached. This convergence factor compares the nodal distortional kinetic energy to the peak distortional kinetic energy of the system. Once convergence is reached, the model is stable and transient analysis can initiate. The following transient analysis uses the end condition of the dynamic relaxation phase as initial conditions[18].

The beam dump is simulated with the following preloads in a dynamic relaxation phase:

- The shrink fit of the graphite blocks in the vessel.
- The internal nitrogen pressure inside of the vessel.
- The application of gravity.
- An initial displacement of the vessel to place it onto its cables before beam impact.

In the transient analysis of the beam dump, the energy deposition of the beam is applied in 86 μs after which the simulation is run for 0.05s to capture the induced vibrational modes.

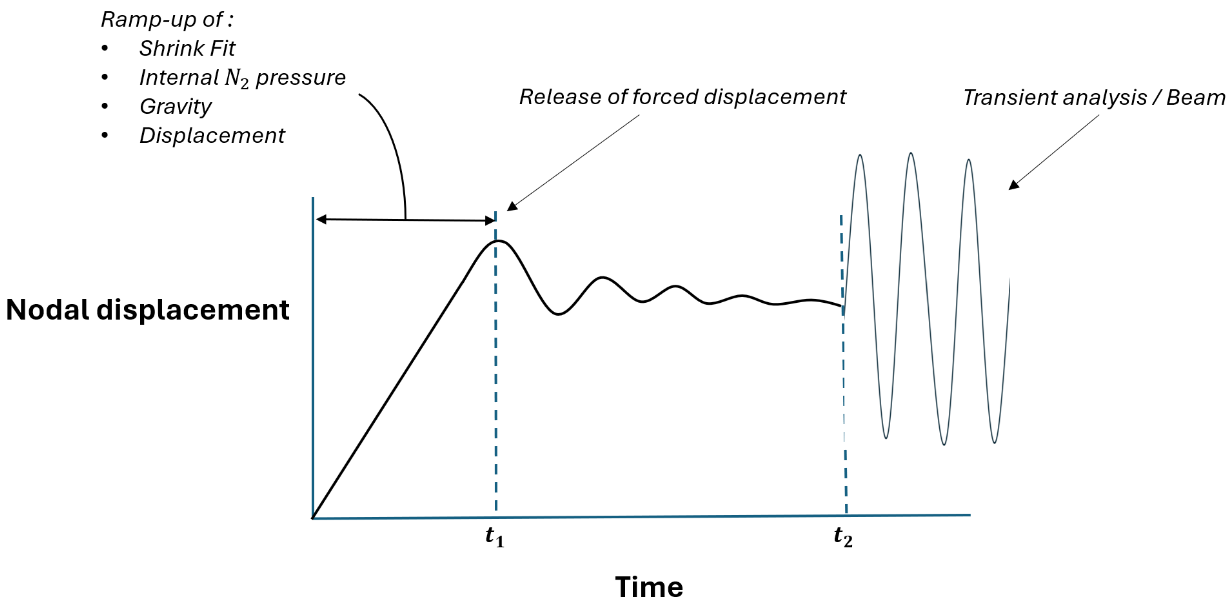

Figure 6.13: Workflow of the dynamic relaxation phase of the beam dump simulation in order to apply the required preloads and establish equilibrium before initiating the transient run.

6.4.1 Gravity and pre-tensioning of cables

To include the prestressed state of the cables as a result of the weight of the dump block, an equilibrium is simulated with dynamic relaxation. A forced displacement is applied onto the vessel for the model to find contact between the vessel and the cables. The selection of an appropriate displacement for the desired pretension of the cables is discussed in appendix A.3.1. As the cableguides come into contact with the cables, the cables are tensioned. The forced displacement is released during the dynamic relaxation phase to allow the model to dampen out the dynamic nodal velocities (see t_1 in figure 6.13). The tensioning of the cables results in reaction forces of the cables. Thus, the vessel tends to rebound on the cables upon the release of the forced displacement. This oscillation is slowly damped out by the dynamic relaxation between t_1 and t_2 shown in figure 6.13. Once the dump block has stabilised sufficiently on the cables and static equilibrium has been found (t_2), dynamic relaxation terminates, and the transient phase can start.

To validate the found state of equilibrium obtained at t_2, the resultant forces in the cables have been calculated by hand. This required the determination of the center of gravity of the dump block. This hand calculation can be found in appendix A.3.3. The simulated axial forces in the cables after dynamic relaxation have been outputted from the simulation and compared with the calculated values in table 6.2.

	Simulated axial force	Calculated axial force	Deviation
Upstream cable	16.8 kN	16.4 kN	2.4%
Downstream cable	15.8 kN	15.1 kN	4.6%

Table 6.2: Comparison between simulated and calculated axial cable force resultants due to beam dump block weight.

6.4.2 Shrink fitting

The vessel of the beam dump is under a constant preload induced by the shrink fit high-density graphite blocks and internal nitrogen pressure. The prestress due to shrink fitting is modelled by the geometric interference between the high-density graphite core and the vessel. A hand calculation has been performed based on the geometrical interference between the geometry of the vessel and the core to validate the vessel stress resulting from the simulated dynamic relaxation phase after convergence. Its results have been listed in table 6.3. The hand calculation can be found in appendix A.3.2.

Simulated stress [MPa]	Calculated stress [MPa]	Deviation [%]
242.3	246.0	1.5

Table 6.3: Comparison of calculated and simulated hoop stress in the vessel due to the shrink fit of graphite blocks.

6.5 Transient run after dynamic relaxation

During the transient analysis, the energy deposition, computed with FLUKA Monte Carlo simulations is applied onto the vessel and the support frame. The energy deposition into the dump core is not included due to the low coefficient of thermal expansion (CTE) of the graphite in respect to the other materials [27] as shown in table 6.4. This does not allow any dynamic phenomena from the beam dump core to propagate to the vessel and interact with the reponse of the vessel. Furthermore, the time of the dynamic response is not large enough to capture any significant heat conduction from the core that could potentially influence the vessel [21]. These simpliciations were validated in previous studies for the Run 2 beam dumps [21]. Neglecting this energy deposition in the model decreases model complexity.

Material	Coefficient of thermal expansion $[K^-1]$
Stainless Steel 318LN	$12.4 * 10^{-6}$
Titanium Grade 5	$8.8 * 10^{-6}$
Sigrafine	$3.6 * 10^{-6}$

Table 6.4: CTE comparison of multiple materials of the TDE dump core [27].

The energy deposition within the frame is overruled by the thermal load taken up by the vessel as visible in table 6.5. The energy deposition onto the support frame is only applied onto its side members, as these carry more than 80 % of the energy deposited in the frame. Remaining margins of the energy intrude into the upstream and downstream cradle, but have been neglected for this analysis.

	Energy deposition [MJ]
Dump block vessel	18.3
Support frame	1.4

Table 6.5: Energy deposition into the vessel and support frame during a 402.1MJ dump with Run 3 beam parameters.

A specific beam dump scenario is simulated. This is the energy level of a recently measured beam dump as its vibrational measurement data is readily available to compare with. It concerns a beam dump of 402.1 MJ. The FLUKA data is delivered as the mean energy deposition of a single proton. The number of protons can be scaled within the simulation interface to reach the energy corresponding with that intensity. As the beam energy level scales linearly with the number of protons, the necessary proton count can be scaled as visible in table 6.6 . This number is used as an input in the analysis.

Scenario	Number of protons	Energy [MJ]
Single proton	1	$1.60 * 10^{-13}$
Measured beam at 07-11-2023	$3.69 * 10^{14}$	402.1
Full intensity beam	$4.95 * 10^{14}$	539

Table 6.6: Comparison of beam intensity and their respective energy for 6.8 TeV protons.

In reality, the individual bunches of particles within the beam are transversely swept across the face of the beam dump during 86 microseconds [22]. This results in a complicated energy distribution that varies both in space but also with time. However, in the simulation the energy deposition of the dumped beam is applied for the first 86 microseconds of the analysis time and is released immediately after. Not accounting for the time dependence of the energy deposition is justified by the very short deposition time that is much smaller than the highest observed vibrational frequency of the beam dump.

Chapter

7 Run 3 Benchmark simulation results

The displacement during longitudinal vibration generated by the model are visualised in figure 7.1. It is apparent that the vessel extends and contracts consecutively in a high frequency oscillation due to an immediate excitation of vibrational modes as a consequence of the beam impact.

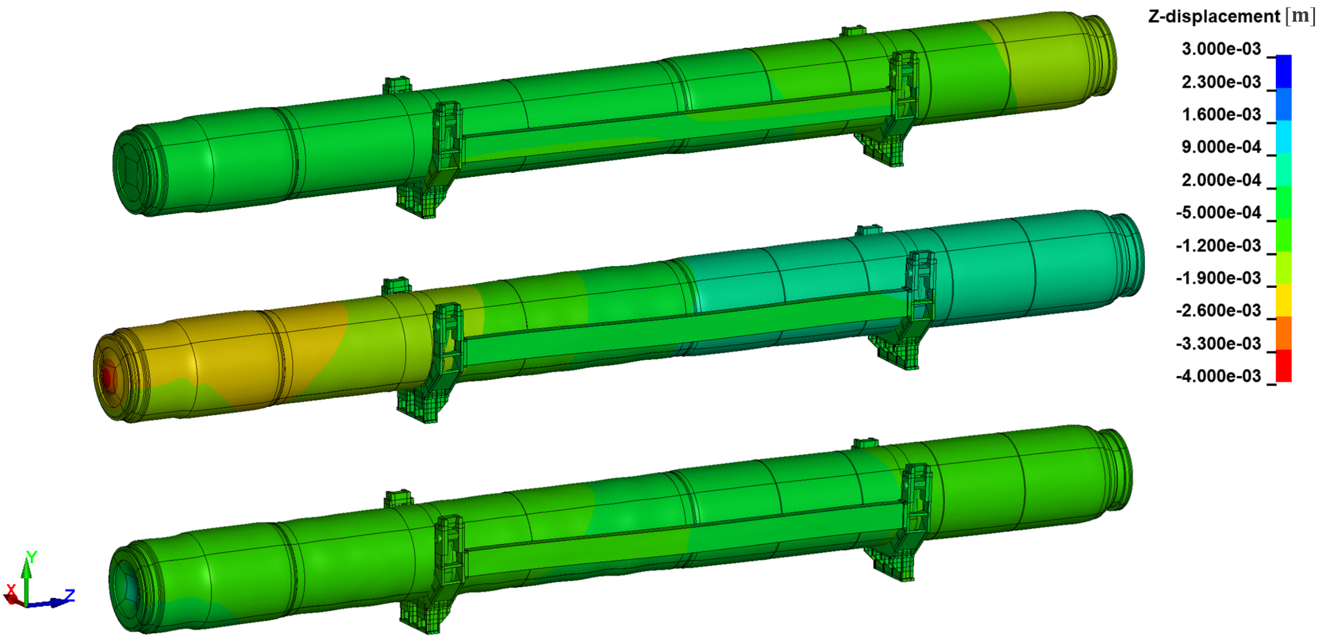

Figure 7.1: Results of simulated longitudinal displacement in meters of the Run 3 beam dump during a 402.1MJ beam dump event, scaled with a factor of 40. Top: displacement before receiving the beam. Middle: expanded displacement 2.6 ms after absorbing beam energy. Bottom: returned position 58 ms after absorbing beam energy.

In this process of vibration, the cables are loaded in tension and allow the vessel to vibrate freely. The cables interact with the vessel cable guides while allowing for free vibrations due to the rapid thermal expansion. Simultaneously they remain tightly connected to the pins of the support frame. The simulated behaviour of the upstream cable is shown in figure 7.2.

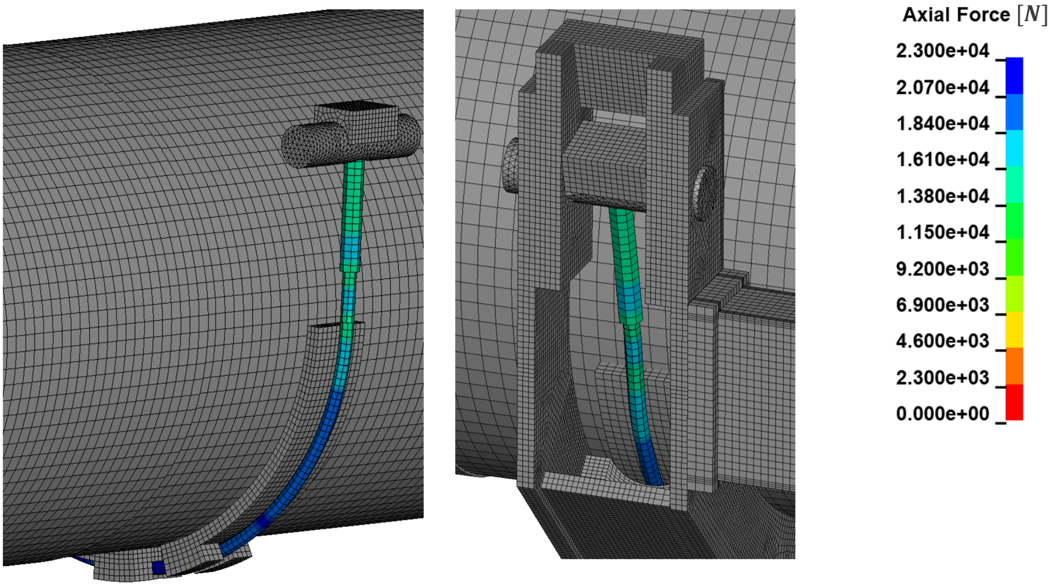

Figure 7.2: Results 25 ms after beam impact of the simulated response of the support frame cables during a 402.1 MJ beam dump event. The axial force within the upstream cable as it interacts with the vessel cable guide, visual deformation is scaled by a factor of 10.

Figure 7.3 showcases the longitudinal movement of the cables taken from nodes located at an identical height on their respective cables. The cables move along with the longitudinal displacement of the vessel. The upstream end of the vessel initially extends in upstream direction and the downstream end extends in the downstream direction. This means that the cables longitudinally displace in anti-phase opposed to each other. Consequently, no swinging movement of the dump block is introduced by the cables.

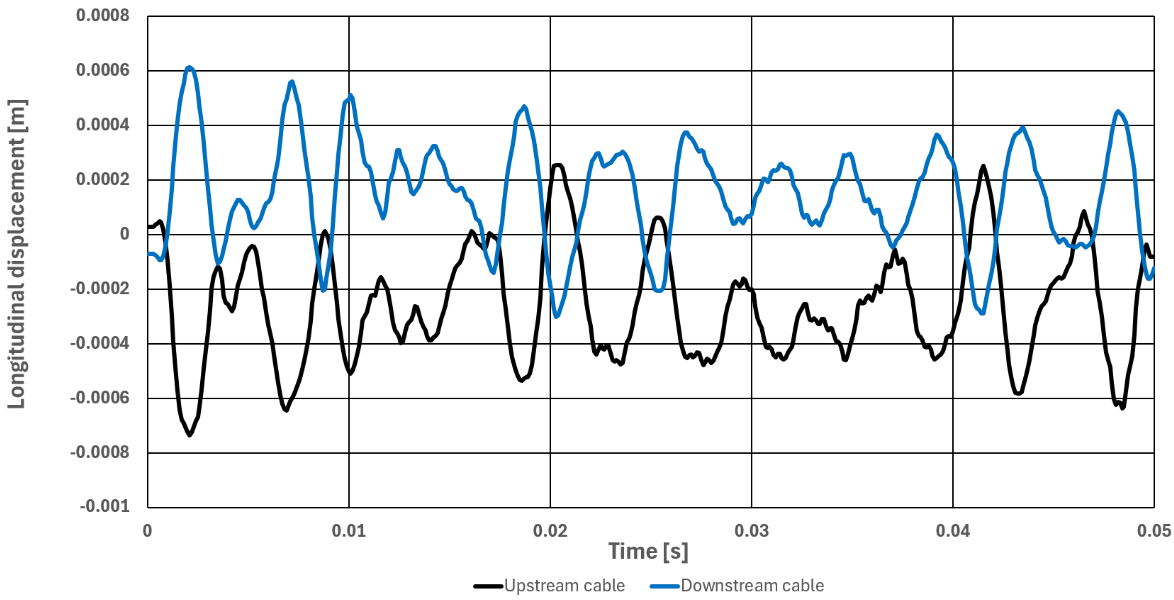

Figure 7.3: Simulated response of longitudinal displacement of both support frame cables over time during a 402.1 MJ beam dump event.

To directly compare the movement of the model with measurement data, a node with a similar position as the measurement point of the LDV is selected. In this case the positive longitudinal direction denotes the downstream direction, and the negative longitudinal direction denotes the upstream direction. The velocity of the longitudinal vibrations generated by the model are shown and compared to measurement data of a 402.1 MJ dump in figure 7.4 and table 7.1.

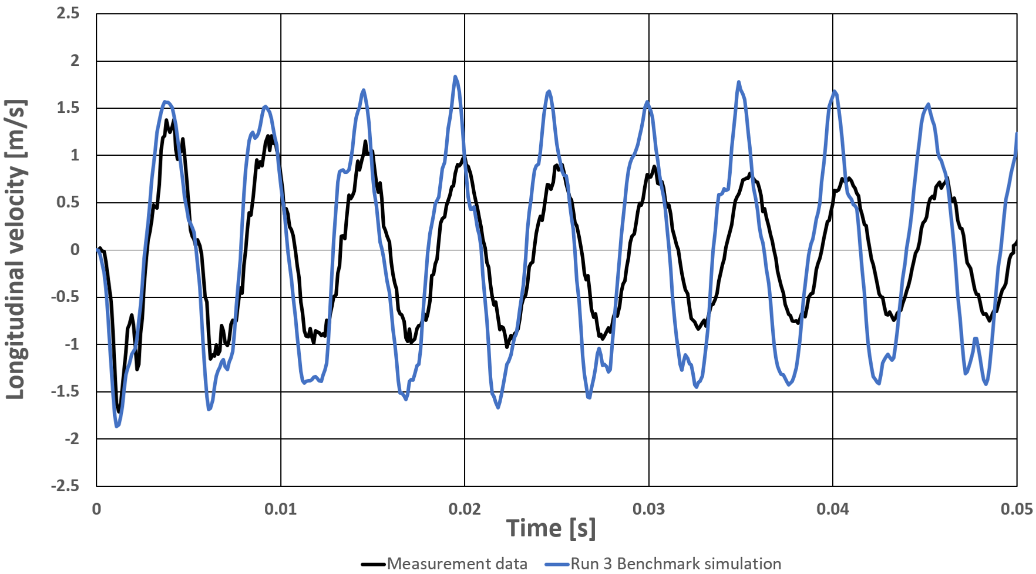

Figure 7.4: Comparison of the Run 3 simulation model and measured longitudinal velocity of the upstream window of the dump block for a 402.1 MJ dump. The simulation model shows strong correspondence in frequency. The resulting amplitude of the first oscillation exhibits an accurate correlation with measurement data. Dampening of the vessel's longitudinal vibration is however not included in the simulation of its response.

	Measurement data	Simulation	Deviation
Frequency	200 Hz	199.5 Hz	0.25%
Amplitude	1.71 m/s	1.87 m/s	9.4%

Table 7.1: Comparison of the frequency and amplitude of the simulated and measured longitudinal velocity of the run 3 TDE during a 402.1 MJ beam dump.

Strong correlation can be seen in the frequency of the vibration induced by the beam impact of 402.1 MJ. The resulting amplitude of the first oscillation exhibits an accurate correspondance with measurement data. However, the dampening of its movement is not yet included. The lack of a damping model in the finite element analysis results in an overestimation of the amplitude of oscillations over time, thereby exaggerating the impact of fatigue on the stress levels in the vessel for potential future studies.

Chapter

8 Cable parameter sensitivity study

Limited knowledge on the material parameters of the beam dump cables forms an uncertainty in the obtained simulation results. As mentioned in section 6.3, simulating the cables requires the specification of three material curves:

- Axial strain to axial force
- Curvature to bending moment
- Rate of twist (R.o.T.) to torque

The necessary curves to describe the behaviour of the cables in bending and torsion are not supplied by the manufacturer. As a result, these parameters would have to be estimated. In order to investigate the effect of the estimated values on the resulting behaviour of the beam dumps, a sensitivity study is conducted. A selection of varying estimated parameters can be applied onto the material assignment of the simulated cables in a range of simulations. The results of this analysis can conclude the degree of uncertainty in results obtained by the lack of these properties. Additionally, the resulting gained knowledge on the effect of these properties on the dynamic behaviour of the beam dump can substantiate the cable selection for future beam dump designs based on their properties.

Two comparable examples of the LS-DYNA simulation of cables with the use of beam elements have been found in literature [26][29]. These include the following cable applications:

- Cables used for the construction of roadside safety barriers [26]
- Cables used in overhead cranes for manufacturing plants [29]

The test data and simulation input data used in these examples is used to estimate cable properties for sensitivity analysis of the beam dump cables. In the case of the roadside barrier cable, all required curves originate from material tests conducted by Midwest Roadside Safety Facility [31]. The simulations conducted for the analysis of overhead crane cable had their curvature-moment curve to be estimated and R.o.T.-Torque relation to be taken from the roadside barrier research [29]. An overview of the known and estimated material relations in literature and for the beam dump cables can be seen in table 8.1.

	Strain - Force	Curvature - Moment	R.o.T. - Torque
Roadside barrier cable	known	known	known
Overhead crane cable	known	estimated	taken from roadside barrier
Beam dump cable	known	to be estimated	to be taken from roadside barrier

Table 8.1: List of useable cable properties of literature examples in order to estimate unknown properties for the beam dump cables [26][29].

8.1 Required cable parameter curves

For both of the unknown curves for the beam dump cables that are required to formulate the beam element, three curves have been formulated and simulated to study their sensitivity.

In both literature cases and the case of the beam dump cable, their strain to force curves are known. Figure 8.1 shows the known cable material strain to force relations, two of which indicate the mentioned literature examples.

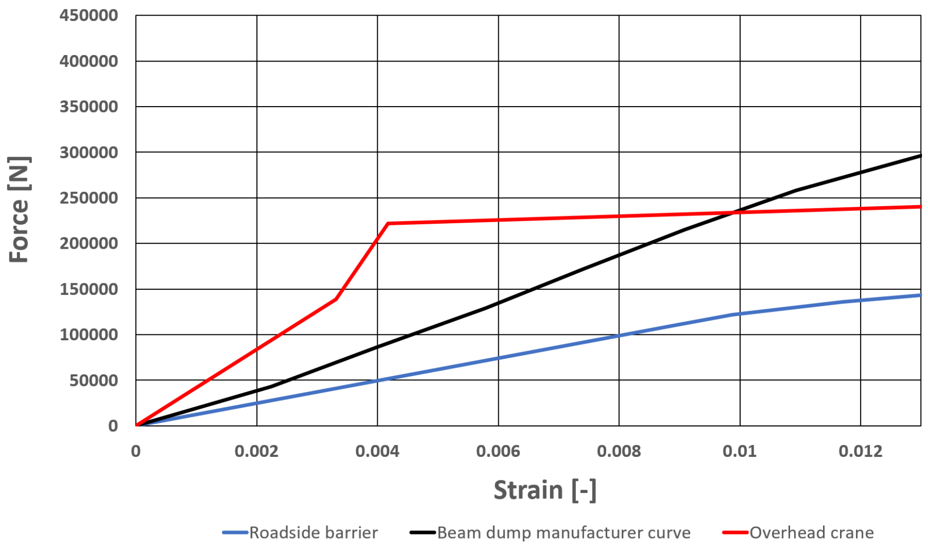

Figure 8.1: Force - Strain relation between two literature examples and the cable used for the beam dump support frame [26][29].

Based on the indicated beam dump cable uniaxial stiffness with respect to the available literature examples, the bending moment to curvature relation has been estimated in relation to those examples as follows in figure 8.2.

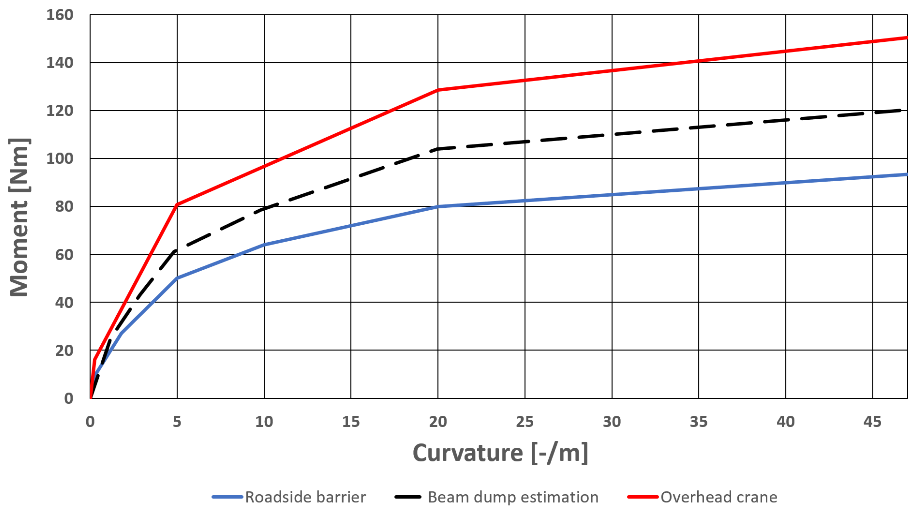

Figure 8.2: Moment – Curvature relation between two literature examples and the estimated curve for the beam dump cable[26][29].

In the analysis of structural wire ropes, only the available literature on roadside barriers has defined a relation between the applied torque and the rate of twist (R.o.T) of a cable[26]. A stiffer and a softer behaviour in torque to rate of twist is estimated to include in the sensitivity study as can be seen in figure 8.3.

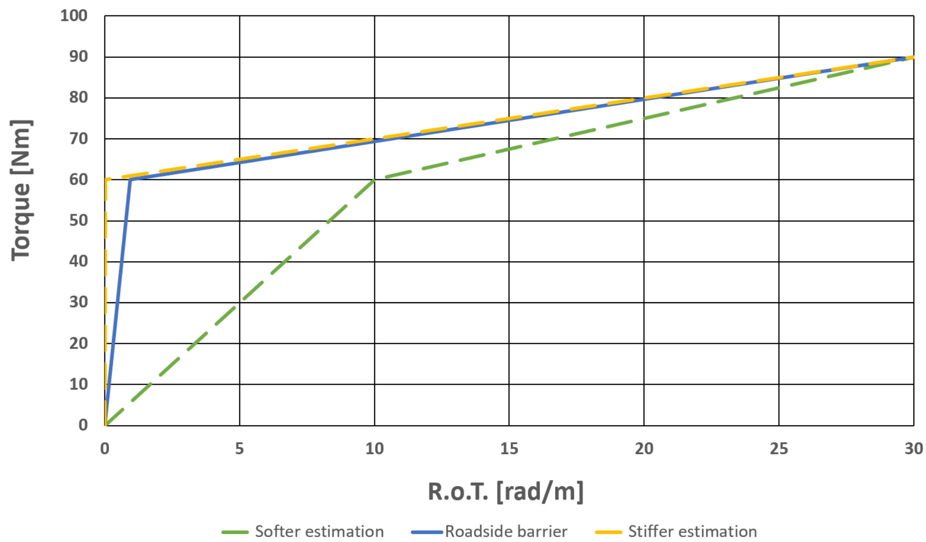

Figure 8.3: Torque - R.O.T. relation taken from literature and two extrapolated examples to be used in the sensitivity study[26].

Six separate vibration simulations are run with varying material properties in curvature-moment and R.o.T.-torque as described in the overview below. The results are generated with a lower output frequency of data points, reducing the resolution of the output signal. However, it reduces the amount of storage needed during post-processing for the sensitivity study, while still delivering results that provide sufficient information about the implications of different cable parameters. All other characteristics of the simulation remain identical as previously described in this thesis.

Variation in bending moment to curvature behaviour (figure 8.2):

- Stiff bending moment-curvature behaviour taken from the overhead crane literature example in figure 8.2 [29].
- Soft bending moment-curvature behaviour taken from roadside barrier literature example in figure 8.2 [26]).
- Estimated bending moment to curvature behaviour as described by the black line in figure 8.2.

Variation in torque to Rate of Twist behaviour (figure 8.3):

- Stiffer torque to R.O.T. behaviour as estimated in figure 8.3.
- Softer torque to R.O.T. behaviour as estimated in figure 8.3.
- Torque to R.O.T. behaviour taken from roadside barrier literature example in figure 8.3 [26].

8.2 Cable parameter sensitivity study results

In figures 8.4 and 8.5 the results of longitudinal vibration of the beam dump are shown with the listed variations in cable properties. As each resulting behaviour follows an identical path, this variation in assigned cable material properties in bending and torsion do not change the simulated vibrational behaviour of the beam dumps.

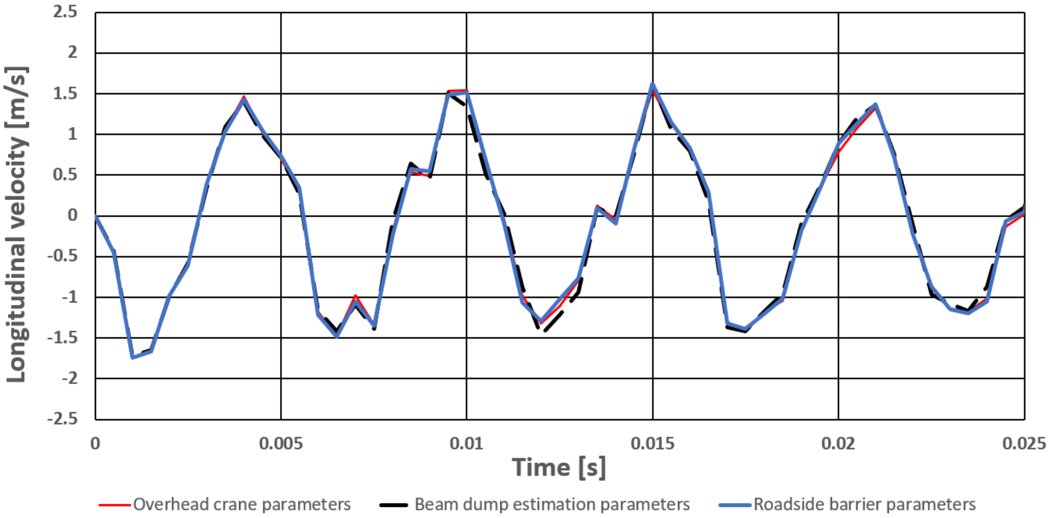

Figure 8.4: Vibration comparison with varying assigned Moment - Curvature relations.

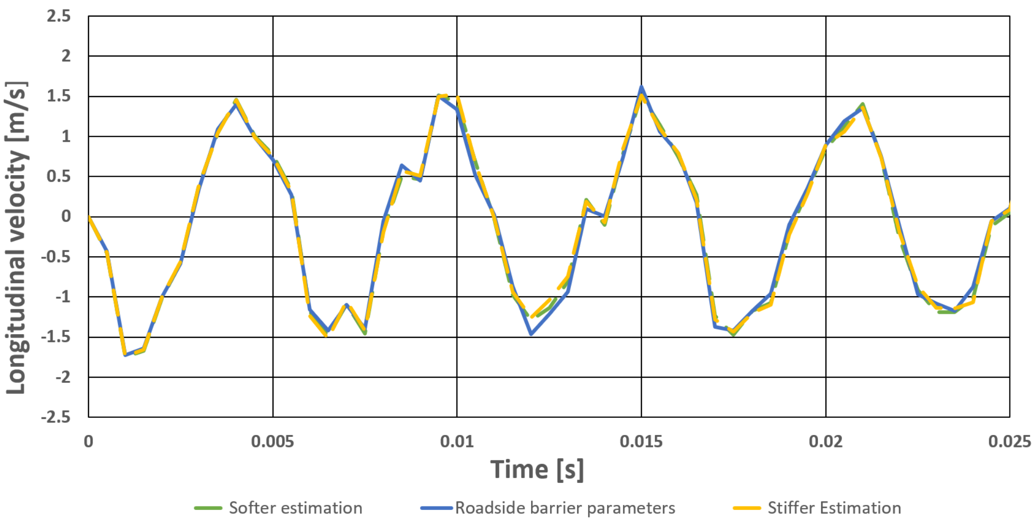

Figure 8.5: Vibration comparison with varying assigned Torque - R.O.T. relations.

The similarity in results despite the differently assigned cable parameters can be explained by the load state of the cables. The cables are mainly loaded in tension and transverse shear and show low resulting internal bending moment and torque as shown in table 8.2.

Axial Force	27 kN
Bending Moment	20 Nm
Twisting Torque	2 Nm

Table 8.2: Simulation results for maximum axial forces, bending moments and torques in the TDE cables

Judging from the relation between these parameters and both the curvature and rate of twist, these values are not large enough to affect the longitudinal vibration behaviour of the TDE. Despite the insecurity in material parameters, the results are not effected by this lack of knowledge. This results in a high confidence in the model results. Furthermore, the acquired knowledge regarding the impact of these characteristics on the dynamic performance of the beam dump can support the selection of cables for upcoming beam dump designs, taking into account the low effect of the researched properties.

Chapter

9 Discussion

The LHC beam dumps initially respond in a highly dynamic manner to beam impact. To address the structural challenges introduced by the dynamic response of these devices, it is crucial to gain an understanding of this behavior through the development of finite element models. However, the simulation model previously developed for dynamic analysis of the Run 2 beam dumps, showed limited agreement with the actual device's vibrational measurement data [21]. Finite element models for the dump block of the Run 3 beam dumps have been developed in past years to perform detailed sub-analyses or to investigate potential design options. However, a model had not yet been developed to benchmark the simulations with sensor measurements to verify its accuracy. The previously stated engineering problem aimed at developing an improved and expanded finite element model to simulate the behaviour of the devices more accurately.

The results of the newly developed finite element model showed longitudinal vibrations of the dump block in its response to beam impact while rapidly expanding and contracting on its support frame cables. These vibrations closely resemble the movement of the dumps as measured by sensor equipment, indicating the validity and accuracy of the developed model.

The beam dumps to be developed for the High-Luminosity upgrade will likely carry over numerous characteristics of the current beam dump design. As a consequence of these design similarities, the validated simulation methodology described in this thesis can form the foundation for the simulation in the design and development for the upcoming generation of these devices.
Although the resulting frequency and initial amplitude of oscillation show to be closely replicating measurement data, the magnitude of the simulated oscillations do not show the damped course which they endure in reality. The required energy rise during the HL-upgrade can pose a challenge to the structural integrity of the new beam-intercepting devices with potentially marginal safety factors [6]. The absence of such a damping model in the finite element analysis overestimates the magnitude of oscillations over time, thus exaggerating the influence of fatigue on the stress levels in the vessel. This overestimation of the effect of vibrational fatigue can decrease exploitable design options for future beam dumps if these designs approach material limits.

As explained, beam dumps are designed to withstand any foreseeable beam intensity extracted from the LHC. This study only validated the model in respect to measurement data for a single beam dump event. In order to increase confidence in the validity of the developed model, numerous additional cases could be simulated to investigate its correspondence with measurement data.

Chapter

10 Conclusion

The aim of this thesis was to develop an improved and expanded finite element model to simulate the behaviour of the Run 3 beam dumps more accurately by including the support frame into a complete simulation work flow. Consequently, the vibrational response in this improved model should show correspondence with measurement data of the operational devices.

For the analysis of this dynamic system, the explicit time integration scheme was used and solved in LS-DYNA. Within this conditionally stable method, close attention must be paid to the mesh quality and size in order to limit the computing time. Therefore, the geometry of all components have been simplified with the aim of controlling an efficient mesh structure.
Contacts between each separate component of the beam dump block and support system have been defined by studying their function and the effect of the contact definition on the vibrational behaviour of the beam dump.
A Belytschko-Schwer beam element formulation was implemented to simulate the behaviour of the steel wire rope as its formulation is proven to show accurate results in the transverse loading of structural cables. Due to a lack of available structural properties of the support frame cables, a sensitivity study was performed to study the influence of these unknown characteristics. This concerned the cable's properties that define their behaviour in bending and torsion.
Dynamic relaxation was used to introduce preloads on the vessel such as the stresses introduced by shrink fitting and the application of internal nitrogen pressure. Furthermore, the dump block was displaced onto its cables and gravity was applied while gradually dampening out nodal velocities. The dynamic relaxation process ensured the obtainment of the construction's equilibrium before applying the thermal load originated by the particle beam.

The newly developed Finite Element model for benchmarking the Run 3 beam dumps showed accurate results in longitudinal vibration compared to the measurement data of a 402.1 MJ dump event. The simulated frequency of vibration showed a high degree of correlation with respect to measurement data. The resulting amplitude of the first oscillation was well captured. However, structural dampening had not been implemented, limiting the detail to be captured in future fatigue calculations.
In comparison with benchmarking efforts performed in the previous generation of LHC-beam dumps, the newly developed model showed a significant improvement in precision as exhibited in table 10.1.

	Run 2 deviation	Run 3 deviation
Frequency	2 %	0.25 %
Amplitude	214 %	9.4 %

Table 10.1: Differences in characteristics of simulated and measured longitudinal velocity vibrations for the Run 2 and Run 3 finite element models of beam dumps during benchmarking simulations [21].

The sensitivity study of the cable characteristics showed that the material properties in bending and torsion do not effect the dynamic behaviour of the beam dumps. The internally occurring bending moment and torque in the cables are too marginal to influence the curvature and twist within the cables. The gained knowledge from this substudy can provide guidance into the selection of cables for the use of the HL-beam dumps.

10.1 Future work

The successful validation of the created model creates various possibilities for further work on both the existing and upcoming beam dumps, as outlined:

- **Run 3 Operational beam dumps**
  - The simulation of the currently operational beam dumps in order to clarify potential operational limits.
- **High-Luminosity beam dumps**
  - The use of the model to simulate High Luminosity (Run 4) conditions as a crucial element in the design development of the new beam dumps to be installed in 2028.
  - The possibility to perform sub-model analysis of the support frame to conduct detailed stress - and fatigue analysis for its structure and welds.
  - The design of the support structure for the High Luminosity beam dumps.

Bibliography

[1] ABAQUS. *22.1.1 Solid (continuum) elements*. 2006. URL: https://classes.engineering.wustl.edu/2009/spring/mase5513/abaqus/docs/v6.6/books/usb/default.htm?startat=pt06ch22s01alm01.html.

[2] Ansys. "Contact Technology Guide". In: (2021).

[3] Ansys. *Discussion of Implicit and Explicit Methods and Time-step Size*. Tech. rep. 2021.

[4] Ansys. *Implicit and Explicit Time Integration Time Integration Method-Lesson 2*. Tech. rep. 2021.

[5] Ansys. *What is Finite Element Analysis (FEA)?* URL: https://www.ansys.com/simulation-topics/what-is-finite-element-analysis.

[6] G Banks et al. "DESIGN DEVELOPMENT AND R&D FOR CERN'S HL-LHC EXTERNAL BEAM DUMP". In: Geneva, 2022. ISBN: 978-3-95450-231-8. DOI: 10.18429/JACoW-IPAC2023-TUPM122.

[7] Giuseppe BATTISTONI et al. "The Application of the Monte Carlo Code FLUKA in Radiation Protection Studies for the Large Hadron Collider". In: *Progress in Nuclear Science and Technology* 2.0 (Oct. 2011), pp. 358–364. ISSN: 2185-4823. DOI: 10.15669/pnst.2.358.

[8] CERN. *LHC the guide*. Tech. rep. Geneva, 2021. URL: http://press.cern/press-kit.

[9] CERN. *The 2016 physics season starts at the LHC*. May 2016. URL: https://home.web.cern.ch/news/press-release/cern/2016-physics-season-starts-lhc.

[10] Dornfeld and W. *Thick-Walled Cylinders and Press Fits*. Fairfield, 2018.

[11] R.C. Hibbeler. *Engineering Mechanics: Statics in SI Units*. 14th edition. London: Pearson, 2016.

[12] R.C. Hibbeler. *Mechanics of Materials*. 10th Edition. London: Pearson, Jan. 2017.

[13] G. Hofman. *Finite Element Method*. Utrecht: Stili Novi, 2016.

[14] Krishan Kumar, Deepam Goyal, and S. S. Banwait. "Effect of Key Parameters on Fretting Behaviour of Wire Rope: A Review". In: *Archives of Computational Methods in Engineering* 27.2 (Apr. 2020). ISSN: 18861784. DOI: 10.1007/s11831-019-09326-y.

[15] A Lechner et al. *Beam-induced energy deposition on dump block assembly*. Tech. rep. Geneva: CERN, 2021.

[16] A. Lechner. "Particle interactions with matter". In: *CERN Yellow Reports: School Proceedings*. Vol. 5. March. CERN, 2018, pp. 47–68. ISBN: 9789290834762. DOI: 10.23730/CYRSP-2018-005.47.

[17] AN ANSYS COMPANY LIVERMORE SOFTWARE TECHNOLOGY (LST). *LS-DYNA® KEYWORD USER'S MANUAL VOLUME 1*. Livermore, Sept. 2021.

[18] LIVERMORE SOFTWARE TECHNOLOGY CORPORATION. "Preloads in LS-DYNA". In: (2003).

[19] A.L. Lund. "Upgrades of the Target Dump Externals for the Large Hadron Collider". In: (Aug. 2022).

[20] Erik Lund and Esben Lindgaard. *Notes for course on Finite Element Methods, 2023 Introduction Motivation for the course Objective of the course 1/2 Objective of the course 2/2 and Evaluation.* Tech. rep. 2021.

[21] J Maestre et al. *CERN LHC External Beam Dumps (TDE) Modifications and upgrades during LS2 for Run3.* Tech. rep. 2021.

[22] J. Maestre et al. "Design and behaviour of the Large Hadron Collider external beam dumps capable of receiving 539 MJ/dump". In: *Journal of Instrumentation* 16.11 (Nov. 2021). ISSN: 17480221. DOI: 10.1088/1748-0221/16/11/P11019.

[23] Andreas Öchsner. *Classical Beam Theories of Structural Mechanics.* Springer International Publishing, Jan. 2021, pp. 1–186. ISBN: 9783030760359. DOI: 10.1007/978-3-030-76035-9.

[24] Optomet. *Measurement Principle - Laser Vibrometry.* URL: https://www.optomet.com/technology/measurement-principle/.

[25] F.S. Pujol. *An introduction to the Monte Carlo method for the simulation of radiation transport.* Sept. 2022. URL: https://cds.cern.ch/record/2827137?ln=en.

[26] John D Reid, Karla A Lechtenberg, and Cody S Stolle. *Development of Advanced Finite Element Material Models for Development of Advanced Finite Element Material Models for Cable Barrier Wire Rope Cable Barrier Wire Rope.* Tech. rep. Nebraska: University of Nebraska, 2010. URL: https://digitalcommons.unl.edu/matcreports.

[27] SGL CARBON GmbH. "SGL-Datasheet-SIGRAFINE-R7300-EN". In: (2019).

[28] SIMULIA. *Structural Elements in Abaqus.* 2014. URL: https://eduspace.3ds.com/CompanionManager/up/?&lexType=1&lang=en&lpId=226375&cls_aud=s&utm_source=18165_5_33&utm_medium=onl_lpt&utm_campaign=P226375&/index.html/#/lp-content.

[29] Andrew Smyth. *Simulation of Overhead Crane Wire Ropes Utilizing LS-DYNA ®.* Tech. rep. New York: LPI, Inc., 2018.

[30] Rende Steerenberg. "Accelerators for Beginners and the CERN Complex". In: (2021).

[31] Cody S Stolle and John D Reid. *Modeling Wire Rope Used in Cable Barrier Systems.* Tech. rep. Nebraska: Nebraska LTAP, 2010.

A Appendix

This appendix predominantly includes details on the setup of the developed finite element model including various calculations and validations. The structure will follow in the following order:

- A.1: Appendix 1 - Geometry preparation and mesh
- A.2: Appendix 2 - Contact Definitions
- A.3: Appendix 3 - Dynamic Relaxation

A.1 Appendix 1 - Geometry preparation and mesh

Before meshing, many details are removed from the model's geometry to improve meshing. Holes and fillets have been removed from its geometry. Hex elements have been used throughout the entire model. The windows and core blocks have been split by applying a square shaped section in the middle of their cylindrical shape as shown in figure A.1. This technique prevents exceptionally skewed elements from forming near the middle of its shape. The mesh of each part is controlled by specifying the number of divisions or element size over its length, circumference, and thickness. This level of control ensures a consistent mesh quality over the entire structure. Other examples are shown in figure A.2 and A.3

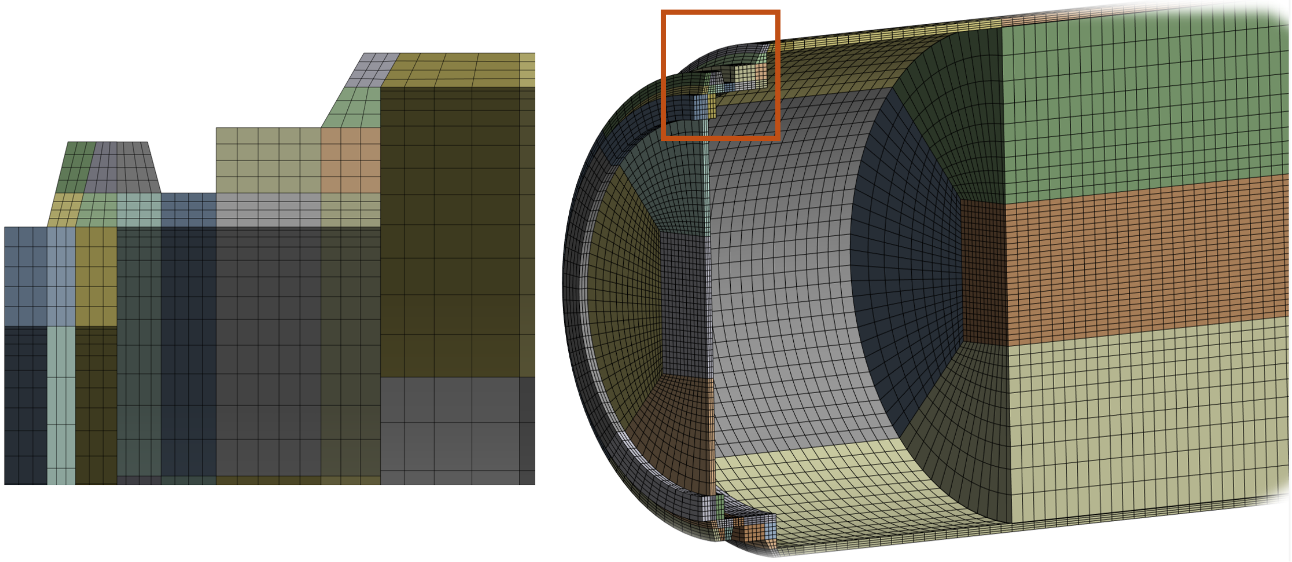

Figure A.1: Left: cross sectional detail view of geometry splits and mesh in the upstream flange and window. Right: cross sectional view of the vessel and core geometry simplification and discretisation.

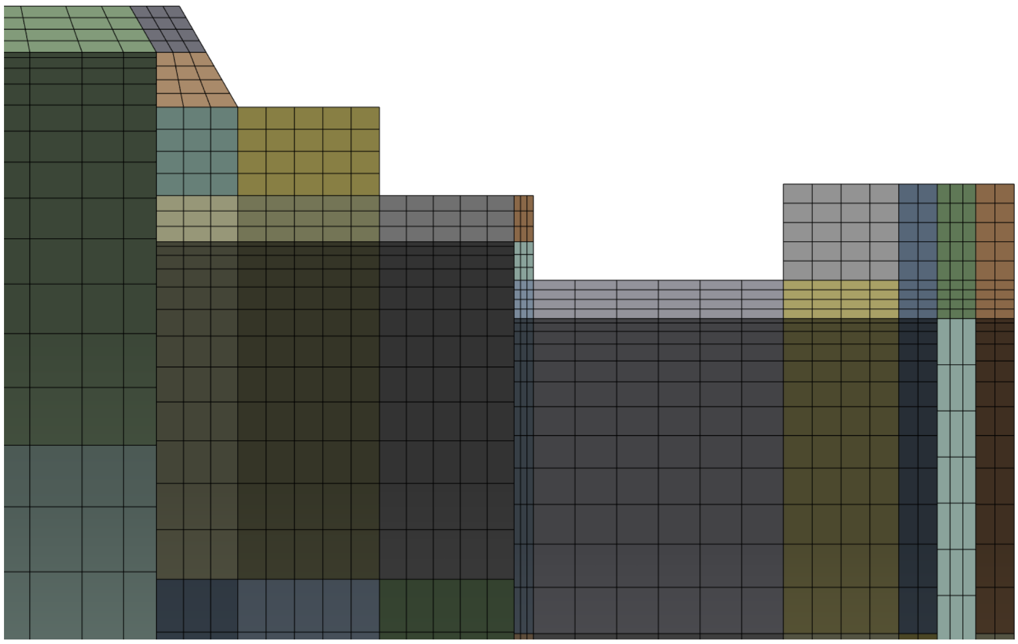

Figure A.2: Geometry simplifications, splits and mesh application of the downstream flange and window.

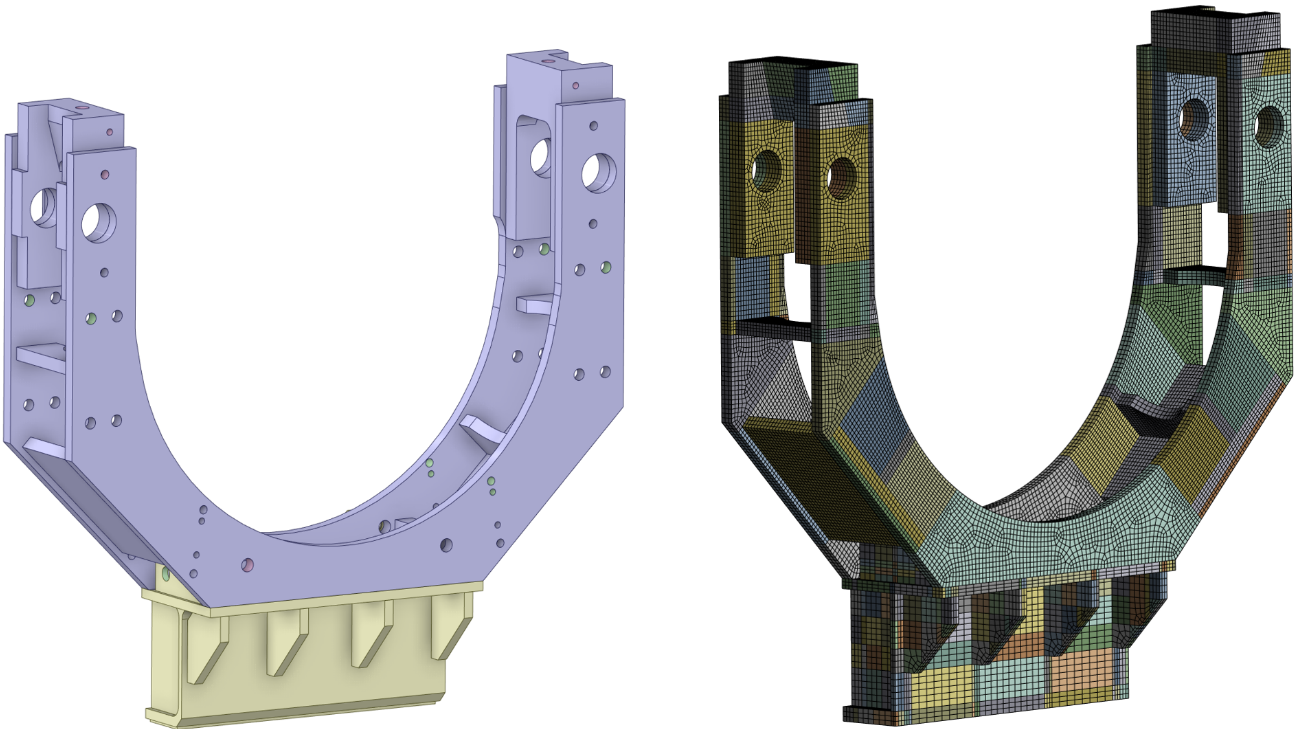

Figure A.3: Support frame cradle geometry simplification and discretisation.

The CFL timestep depends on the characteristic length of the smallest element within the entire structure. This characteristic length is found in the pins of the support frame. Due to its round shape and hole through which the cable protrudes, the geometry is too complex to apply hexahedral elements.Thus, tetrahedrons are used as shown in figure A.4. The skewed shape of a number of these elements leads to the characteristic length that controls the time step of the simulation model shown in table A.1.
Its mesh size has been balanced in such a way that a selection of larger elements would lead to lower quality and thus a skewness leading to a smaller characteristic length, while a selection of smaller elements would lead to smaller characteristic lengths due to size reduction.

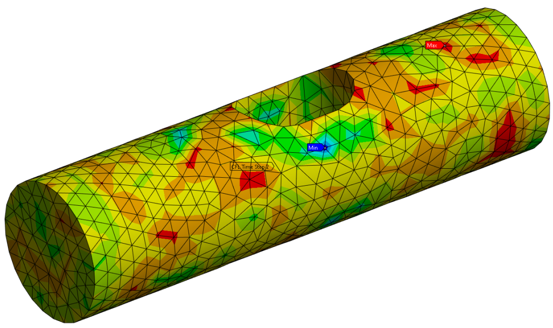

Figure A.4: Support frame pin CFL parameters on mesh. The blue color indicating the smallest CFL time step.

Number of elements	CFL time step [s]	Required simulation time [h]
1278782	$2.1 * 10^{-7}$	7.5

Table A.1: Mesh and CFL information of the TDE simulation model

A.2 Appendix 2 - Contact Definitions

The following table and images indicate the contacts used and their location of application in the simulation of the beam dump. Contact friction coefficients (c_f) have been taken from previous simulation efforts [21]. In the past the sensitivity of the results on varying friction coefficients has been tested and showed very little variety in results [21].

Index nr.	Contact surface	Target surface	Contact type	Static c_f	Dynamic c_f
1	HD Graphite	Vessel	Interference with friction	0.5	0.35
2	LD Graphite	Vessel	Frictional	0.1	0.07
3	HLM Graphite	Vessel	Frictional	0.5	0.35
4	LD Graphite	HLM Graphite	Frictional	0.5	0.35
5	Window	Vessel Flange	Bonded	-	-
6	Cable guide	Vessel	Bonded	-	-
7	Retaining ring	Vessel	Bonded	-	-
8	Retaining ring	HLM Graphite	Frictional	0.5	0.35
9	Side member	Cradle	Bonded	-	-
10	Cradle foot	Cradle	Bonded	-	-
11	Cable	Vessel	Frictional	0.6	0.42

Table A.2: Position and numbering of contact interactions of the TDE dump block.

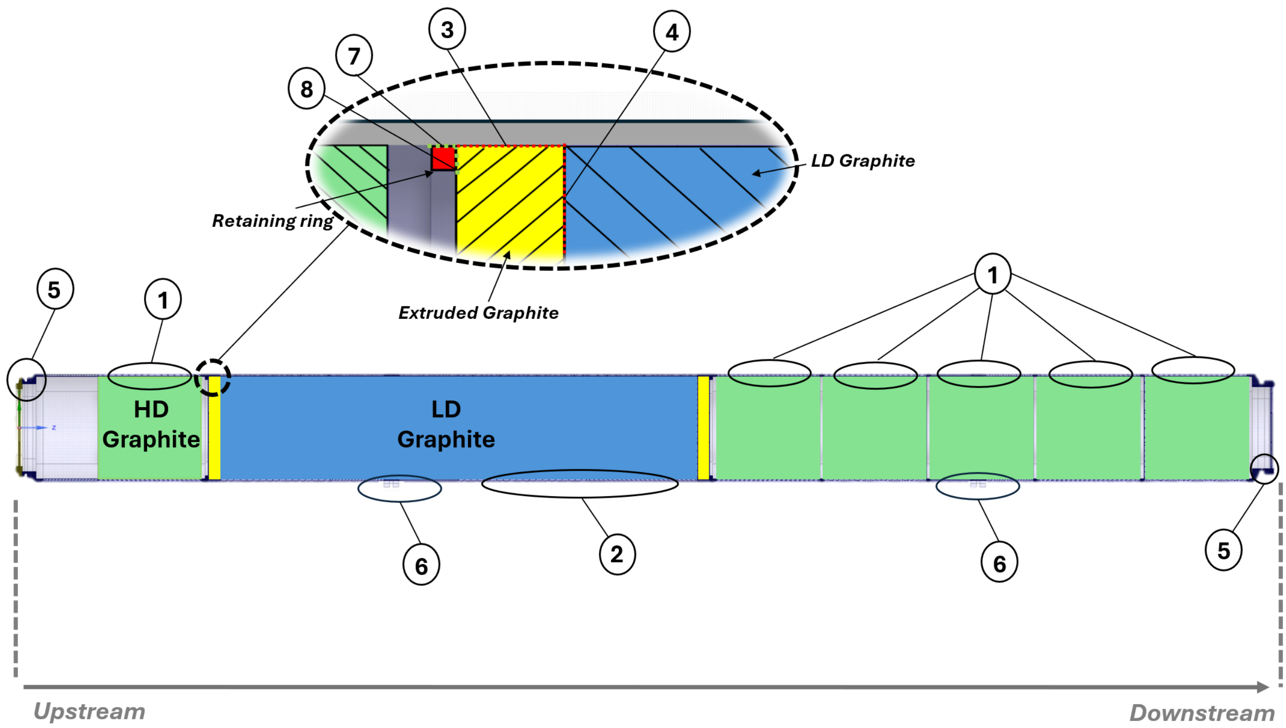

Figure A.5: Position and numbering of contact interactions of the TDE dump block.

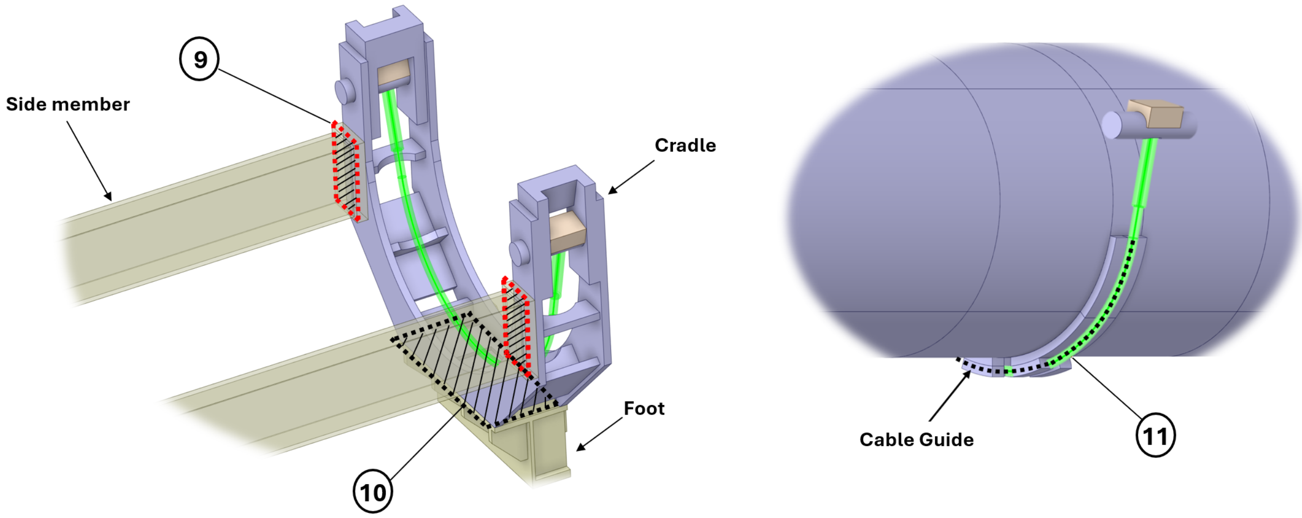

Figure A.6: Position and numbering of contact interactions of the support frame.

The surface assignment of the contact (slave) and target (master) side has been performed by following some of the main contact definition guidelines stated by Ansys [2]:

- If there is a difference in stiffness of both surfaces the stiffer surface should be treated as the target surface.
- If one surface has a finer mesh than the other involved surface, the coarser mesh should be the target surface.

A.3 Appendix 3 - Dynamic Relaxation

Prior to applying the beam energy to the TDE, dynamic relaxation is utilized on the model. This process takes into account preloads on the vessel, including stresses from shrink fitting and internal nitrogen pressure. Additionally, the dump block is displaced onto its cables, gravity is applied. In this DR-phase node velocities are gradually reduced to achieve equilibrium.

This appendix motivates the choices made to set up the dynamic relaxation phase and validates the results of the dynamic relaxation results regarding:

- The prestress due to shrink fitting in the vessel
- The cable force after reaching equilibrium.

Two important parameters have to be set to control the convergence of the DR phase. The DR factor denotes the reduction factor of nodal velocities in each time step [18]. The convergence tolerance denotes the ratio between the maximum distortional kinetic energy in the system and the peak kinetic energy. Once this tolerance has been met, dynamic relaxation terminates [18]. An iterative process has been performed to investigate a satisfactory converging result in the DR-phase.
The following table shows the chosen parameters for the DR-phase.

DR-factor	0.99999
Convergence tolerance	$1.5 * 10^{-6}$

Table A.3: Parameters chosen for the control of DR-conversion

A.3.1 Determination of displacement

The amount of displacement to apply onto the dump block is an essential decision. When displaced too far, the cables will spring back after releasing the displacement, initially leaving the system to be overly dynamic. When displaced too little, contact between the vessel and cables may not be properly found.

In order to find balance between these two scenarios, the dynamic relaxation has first been performed while gradually applying a large displacement of 2mm to prestress the cables. The displacement has been monitored at which sum of the vertical components of axial forces both in both cables matches to the weight of the dump block as shown in figure A.7. This balance is reached after roughly 0.82mm of vertical displacement.

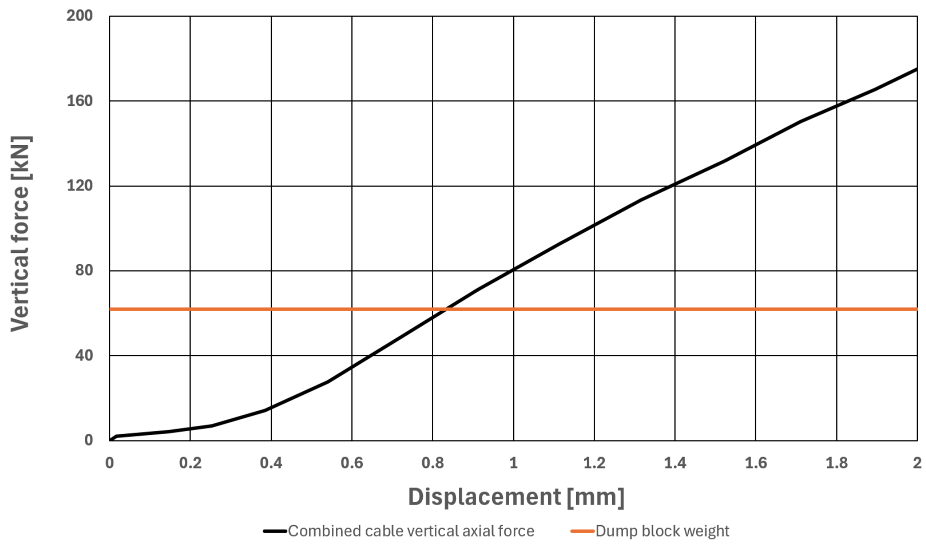

Figure A.7: Simulated vertical component of axial cable force compared to dump block weight to find an appropriate forced displacement in DR

As the total weight of the dump block was calculated by hand as described in appendix A.3.3, a safety margin is introduced on top of the vertical displacement that has been determined. For this reason a vertical of 1mm is chosen to displace the vessel during DR.

Separate displacements have been applied to both the upstream and the downstream end in order to place the dump block onto its cable. This is necessary as the downstream cable of the support frame comes into contact with a prestressed sector of the vessel due to shrink fitting. When the displacement of 1 mm would be added on top of the shrink fitting displacement, the downstream cable force would greatly exceed the equilibrium force necessary. The displacement due to shrink fitting has been subtracted from the applied vertical displacement in DR on the downstream end of the vessel. A schematic representation of this principle has been shown in the images below.

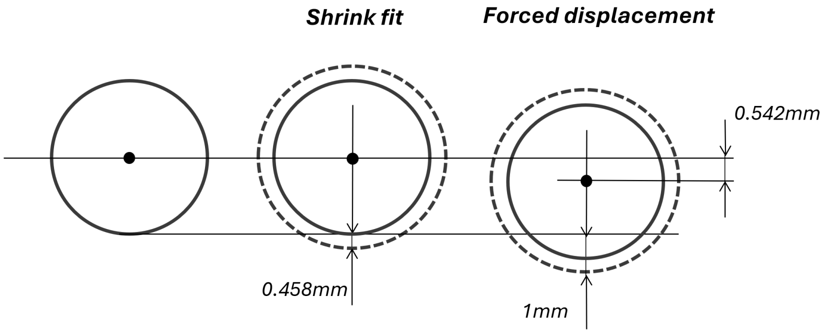

Figure A.8: Front view of the TDE vessel showing the definition of the downstream forced displacement during dynamic relaxation by subtracting the displacement due to shrink fitting.

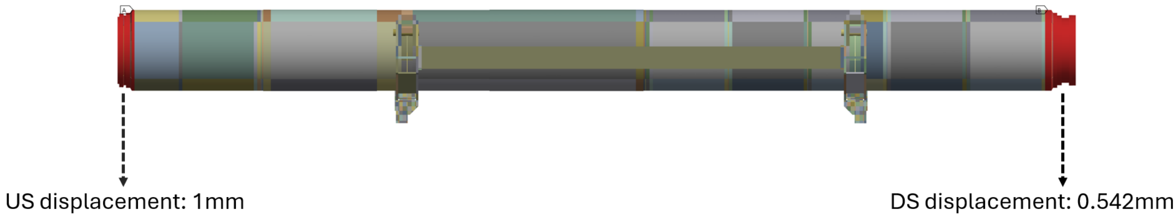

Figure A.9: Defined upstream and downstream displacement of the dump block during dynamic relaxation

This leads to the forced displacement applied to the upstream and downstream window and flange shown in figure A.10.

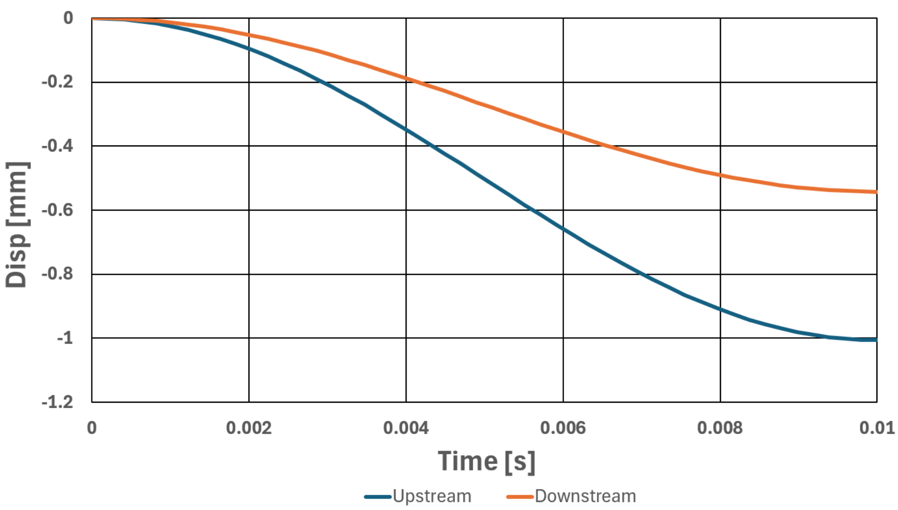

Figure A.10: Upstream and downstream displacement of the dump block onto the support frame cables over the DR time.

A.3.2 Shrink fitting simulation validation

The image below shows the resulting stresses in the vessel after being prestressed in the dynamic relaxation phase. Note that a scale factor of 40 has been applied to emphasise the results. It is clearly visible that only the high-density blocks of graphite create a prestress in the vessel due to their interference.

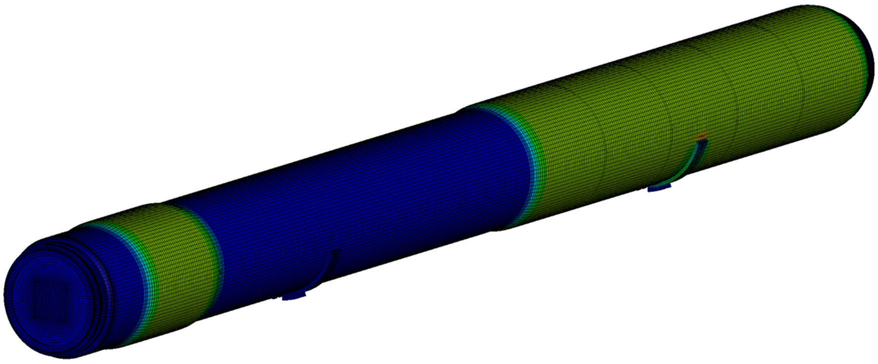

Figure A.11: Stress results of the TDE dump block after dynamic relaxation, showing interference fit stress.

To calculate the vessel stress due to the interference the interference pressure is calculated by using the formula A.3.2 [10]:

$$p = \frac{\delta_r}{\frac{R}{E_o}\left(\frac{r_o+R^2}{r_o-R^2}+\nu_o\right)+\frac{R}{E_i}\left(\frac{R^2+r_i^2}{R^2-r_i^2}+\nu_i\right)} = 8.45\,[\text{MPa}] \tag{A.1}$$

Where

- p is the interference pressure
- δ_r is the difference in radius between the vessel and the graphite core $= 0.75[mm]$
- R is the outside radius of the graphite core = 350 [mm]
- E_o is the young's modulus of the 318LN stainless steel vessel $= 195.2 * 10^3$ [MPa]
- r_o is the outside radius of the vessel = 361.25 [mm]
- ν_o is the poisson ratio of the vessel = 0.31
- E_i is the young's modulus of the graphite core $= 10 * 10^3$ [MPa]
- r_i is the inner radius of the core = 0 [mm]
- ν_o is the poisson ratio of the graphite core = 0.1

After the interference pressure is known, the hoop stress in the vessel is calculated with formula A.3.2 [12]:

$$\sigma_\theta = \frac{p \cdot r_i}{t} = 246.0\,[\text{MPa}] \tag{A.2}$$

Where

- σ_θ is the hoop stress in the vessel [MPa]
- t is the thickness of the vessel = 12 [mm]

The comparison of the simulated and calculated vessel hoopstress can be seen in the table below.

Simulated stress [MPa]	Calculated stress [MPa]	Deviation [%]
242.3	246.0	1.5

Table A.4: Comparison of calculated and simulated hoop stress in the vessel to the shrink fitted graphite blocks.

A.3.3 Cable force simulation validation

The force within the cables in the dynamic relaxation phase is plotted over time in figure A.12. It is visible that the cables respond dynamically during the displacement of the dump block onto the cables. This dynamic movement is slowly dampened out over time until the convergence factor is reached.

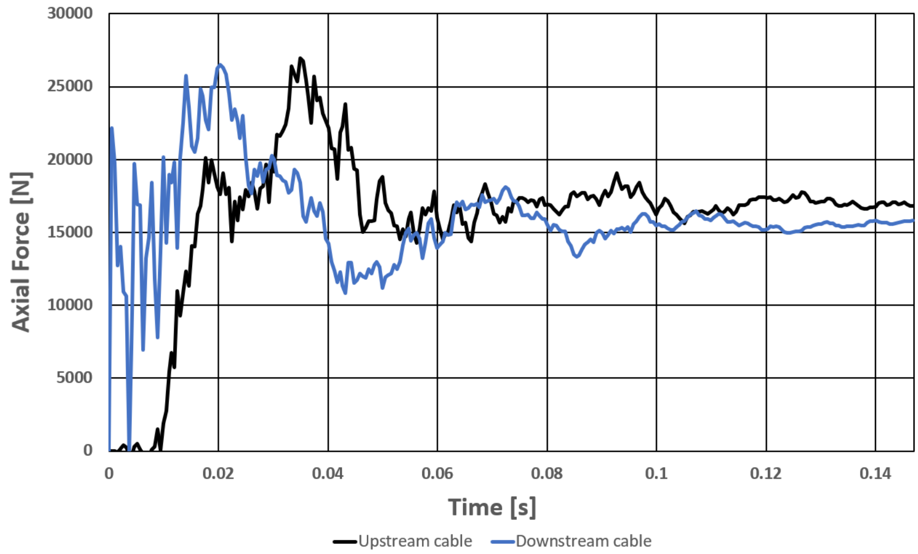

Figure A.12: Simulated axial force in both cables over the pseudo time of the dynamic relaxation phase of the analysis.

Table A.5 shows the simulated axial force within both the upstream and the downstream cable in static equilibrium after reaching convergence in the dynamic relaxation phase.

	Simulated axial force [kN]
Upstream	16.8
Downstream	15.8

Table A.5: Simulation results of the axial cable forces after converging in the dynamic relaxation phase.

The centre of gravity of the TDE dump block is determined to define the tension of the cables in equilibrium of the block itself. This resulting internal cable force can verify the results of the dynamic relaxation phase of the simulation. Figure A.13 shows the positions of each individual component. A detail to be noted are two thickened sections of the vessel. The vessel is thickened in two separate regions positioned around the low-density sector of the core. Their weight contributes to the weight of the dump block and the position of the centre of gravity.

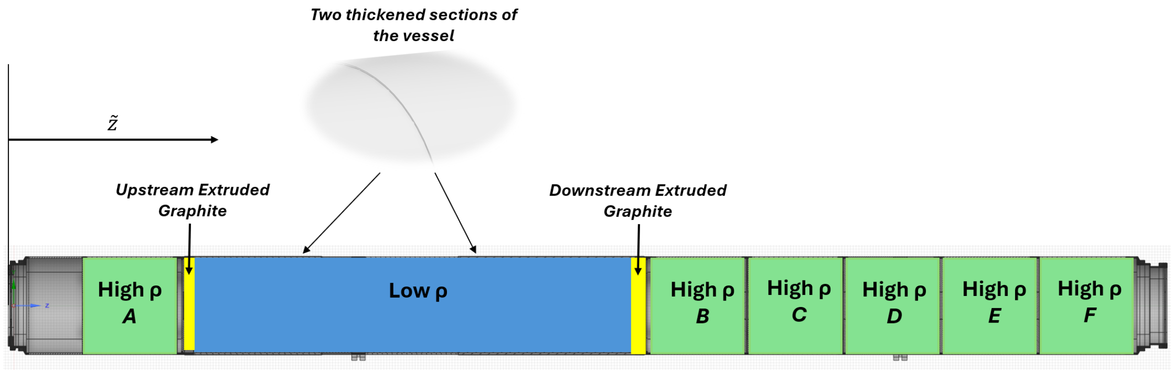

Figure A.13: Location of individual components for the determination of the dump block centre of gravity.

Using the individual centre of gravity of each component the dump block's longitudinal centre of gravity can be calculated with formula A.3.3 [11].

$$\bar{z} = \frac{\sum(m * \tilde{z})}{\sum m} = 4.49\,[\mathrm{m}] \tag{A.3}$$

Where

- $\bar{z}$ = TDE Dump Block centre of gravity [m]
- m = Component mass [kg] (see table A.6)
- $\tilde{z}$ = Longitudinal distance from upstream window to component centre of gravity [m] (table A.6)

Component	**Location**	**Inner ⌀ [m]**	**Outer ⌀ [m]**	**Depth [m]**	**m [kg]**	$\tilde{z}$ **[m]**
Vessel		0.6985	0.7225	8.5	1776	0.01
	Thick section US	0.7225	0.7285	1.015	54	1.793
	Thick section DS	0.7225	0.7285	1.375	73	3.993
HD graphite	A	0	0.7	0.7	466	0.532
	B	0	0.7	0.7	466	4.734
	C	0	0.7	0.7	466	5.442
	D	0	0.7	0.7	466	6.15
	E	0	0.7	0.7	466	6.858
	F	0	0.7	0.7	466	7.566
LD graphite		0	0.696	3.26	1487	1.353
HLM Graphite	Upstream	0	0.696	0.08	66	1.273
	Downstream	0	0.696	0.08	66	4.613
Window	Upstream	0	0.66	0.01	15	0
	Downstream	0	0.63	0.01	14	8.519

Table A.6: TDE Dump block individual component location and measurements.

Individual component masses are calculated with densities mentioned in the following table:

Component	**Material**	**Density** $[kg/m^3]$
Vessel	Stainless-Steel 318LN	7800
HD graphite	SiGRAFINE	1730
LD graphite	SIGRAFLEX sheets	1200
Extruded Graphite	HLM SiGRAFINE	1730
Windows	Titanium grade 5	4430

Table A.7: TDE Dump block individual component materials and densities.

With the known location of the centre of gravity, the individual cable force can be calculated with the help of a free body diagram (figure A.14) and obtaining static equilibrium with the following formulae.

$$W_{tot} = \sum m * g \tag{A.4}$$

$$\sum M_A = W_{DS} * c - W_{tot} * (a - b) = 0 \tag{A.5}$$

$$\sum F_y = W_{US} + W_{DS} - W_{tot} = 0 \tag{A.6}$$

Where:

- W_{tot} = the total weight of the dump block [N] (figure A.14).
- g = earth's gravitational constant = 9.81 $[m/s^2]$ [11].
- $\sum M_A$ = the sum of the moments around imaginary point "A" in figure A.14 [Nm]
- W_{DS} = the vertical component of the weight that is supported by the downstream cable [N] (figure A.14).
- W_{US} = the vertical component of the weight that is supported by the upstream cable [N] (figure A.14).
- a = the longitudinal distance from the upstream window to the dump block centre of gravity = 4.49 [m] (figure A.14).
- b = the longitudinal distance from the upstream window to the upstream cable = 2.57 [m] (figure A.14).
- c = the longitudinal distance between the upstream and downstream cable = 4 [m].
- $\sum F_y$ = the sum of all vertically directed forces in the free body diagram of figure A.14 [N].

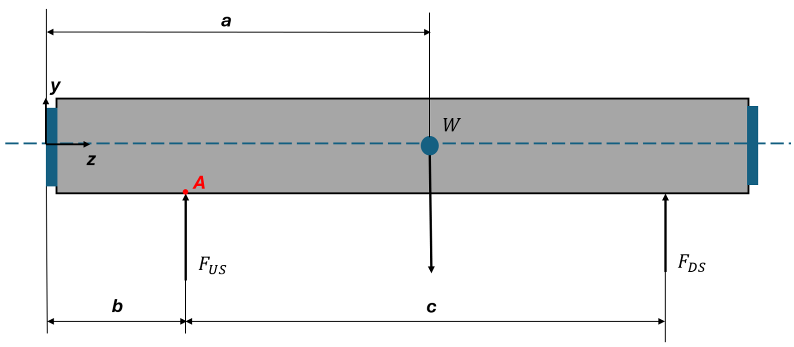

Figure A.14: Free body diagram of the dump block to calculate cable forces.

The following table shows the calculated weight supported by both cables as shown in the free body diagram in figure A.14:

W_{US}	32.2 [kN]
W_{DS}	29.8 [kN]

Table A.8: Calculated weight support by the upstream and downstream cable in equilibrium of the dump block.

From these resulting weights, the individual axial cable force in equilibrium of the dump block can be calculated. A two-dimensional free body diagram has been drawn of the upstream and downstream sectors of the vessel connected to the cables (figure A.15).

The cable forces can be found by solving the following equations of static equilibrium.

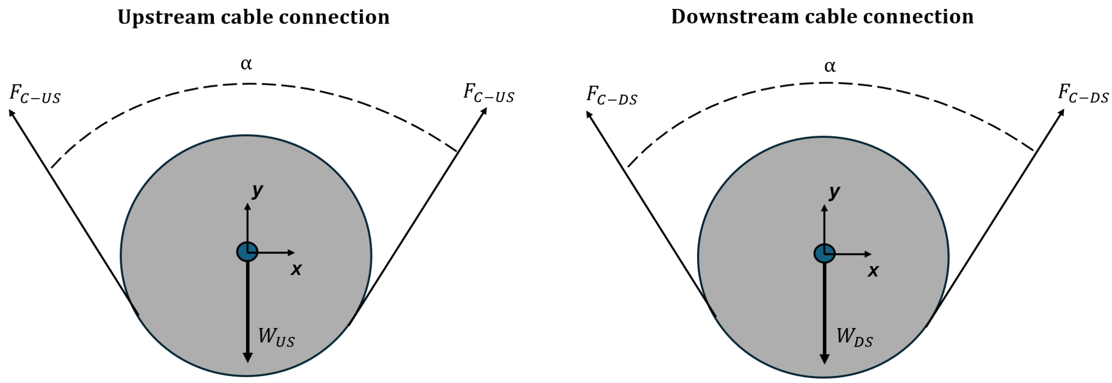

Figure A.15: Free body diagram of static equilibrium at the upstream and downstream cable connection of the beam dump block.

$$\sum F_y = 2 * F_{C-US} * \frac{1}{2}\cos(\alpha) - W_{US} = 0 \quad \text{(A.7)}$$
$$\sum F_y = 2 * F_{C-DS} * \frac{1}{2}\cos(\alpha) - W_{DS} = 0 \quad \text{(A.8)}$$

Where:

- $\sum F_y$ = the sum of all vertically directed forces in the free body diagram of figure A.15 [N]
- F_{C-US} = the axial force within the upstream cable [N] (figure A.15).
- F_{C-DS} = the axial force within the downstream cable [N] (figure A.15).
- α = the geometric angle between both cables = 21.7 ° (figure A.15).

The following table shows the solutions of the axial forces in the cables of the abovementioned equations compared to the simulation results after converging in the dynamic relaxation phase.

	Simulated axial force [kN]	**Calculated axial force [kN]**	**Deviation [%]**
Upstream	16.8	16.4	2.4
Downstream	15.8	15.1	4.6

Table A.9: Calculated cable axial forces from static equilibrium of the dump block compared to the simulated axial force in dynamic relaxation.